5-2021

Optically Active Rare-Earth Doped Films Synthesized by Pulsed Laser Deposition for Biomedical Applications

Charles William Bond
cbond4@vols.utk.edu

To the Graduate Council:

I am submitting herewith a dissertation written by Charles William Bond entitled "Optically Active Rare-Earth Doped Films Synthesized by Pulsed Laser Deposition for Biomedical Applications." I have examined the final electronic copy of this dissertation for form and content and recommend that it be accepted in partial fulfillment of the requirements for the degree of Doctor of Philosophy, with a major in Biomedical Engineering.

Jacqueline A. Johnson, Major Professor

We have read this dissertation and recommend its acceptance:

Russel L. Leonard, Claudia J. Rawn, Feng-Yuan Zhang

Accepted for the Council:

Dixie L. Thompson

Vice Provost and Dean of the Graduate School

(Original signatures are on file with official student records.)

Optically Active Rare-Earth Doped Films Synthesized by Pulsed Laser Deposition for Biomedical Applications

A Dissertation Presented for the

Doctor of Philosophy

Degree

The University of Tennessee, Knoxville

Charles William Bond

May 2021

DEDICATION

I dedicate this work to my family.

ACKNOWLEDGEMENTS

I would like to express my sincere appreciation to my advisor, Dr. Jacqueline Johnson, for giving me the opportunity to do research at the University of Tennessee Space Institute, which allowed me to continue my education while being close to my family. Her generosity and support have helped me to grow in many ways, and this dissertation is a product of that.

I would like to express my gratitude to my committee co-chair, Dr. R. Lee Leonard, for his guidance during this endeavor. He has served as a mentor to me since I began. Through many hours in the laboratory, long meetings, and movie references I did not know, he has helped me grow as a researcher and in many other ways.

I would like to thank Dr. Claudia Rawn and Dr. Feng-Yuan Zhang for their participation in my Dissertation Committee.

The research presented in this dissertation was a collaborative process that gave me the privilege to work with many different researchers. The specific contributions of each collaborator are acknowledged at the beginning of each experimental chapter.

I would like to thank all students, summer interns, faculty, and staff at UTSI that have made my time at UTSI so enjoyable. I especially thank my fellow BEAMS groupmates for their help and laughs throughout the years. Also, the technical assistance of Alexander Terekhov and Douglas Warnberg has been invaluable.

My time at UTSI has given me the opportunity to work with many outstanding researchers from other institutions. Special mention goes to Dr. Amanda Petford-Long from Northwestern University, Dr. Rosalia Serna and Dr. Jose Gonzalo from the CSIC Institute of Optics, and Dr. Richard Lubinsky from SUNY, Stony Brook.

I would like to thank Yu Jin from Northwestern University for working with me through many different projects. Her microscopy expertise was invaluable and gives great detail to the work in this dissertation.

I would like the thank the Laser Processing Group from the CSIC Institute of Optics, who allowed me to come as a visitor to their laboratory. I have thoroughly enjoyed our collaboration and I am appreciative of their generosity.

All projects in this dissertation were supported by the National Science Foundation under grant numbers DMR 1600783 and DMR 1600837

The projects described in CHAPTER II and III were supported by the Spanish Research Council under grants LINKA20044 and RTI2018-096498-B-100 (MCIU/AEI/FEDER, UE).

ABSTRACT

Optically active materials are used in many biomedical applications ranging from medical imaging to light therapies. Investigating the effects of differing nanostructure configurations on the optical performance of these materials can improve tunability, efficiency, and practicality for their respective applications. This work utilizes pulsed laser deposition (PLD) to develop nanostructured thin films and determines their optical performance for applications in computed radiography for medical imaging and in LEDs which can be used in biomedical applications such as photobiomodulation.

In computed radiography, scattering of the stimulation light by the storage phosphor crystal grain boundaries in imaging plates negatively impacts spatial resolution. Storage phosphor plates with thinner phosphor layers have been developed to reduce scattering distance and increase spatial resolution, although at the expense of reduced x-ray absorption. A transparent or translucent nanostructured film, containing a much higher percentage of storage phosphor crystals achievable in bulk glass-ceramic materials made by conventional methods, may have acceptable photostimulated luminescence efficiency and imaging performance characteristics greater than commercial imaging plates. In an attempt to achieve a nanostructured film with superior performance in x-ray imaging, a glass-ceramic imaging plate for computed radiography was synthesized via PLD for the first time. The imaging plate was comprised of Eu-doped $BaCl_2$ crystallites and an amorphous matrix.

Nanolayered films comprising of BaF_2, Eu_2O_3, and Al_2O_3 were synthesized via PLD with differing layered configurations to manipulate the coordinate surrounds of the europium dopant and determine its effects on optical properties. TEM cross-section analysis was conducted to verify the desired nano-layering. Different post-deposition heat treatments were investigated, and the films were evaluated for applications as a phosphor layer for UV-pumped white light LEDs which can be used for solid-state lighting and biomedical light therapies. A Mn dopant was added to europium to discover the threshold for the amount of manganese necessary to optically influence the nanolayered films. Although

Mn/Eu co-doping did not prove advantageous for white light LEDs, all nanostructures of Eu-doped films have the potential for the desired application.

Nanoscale control of optically-active thin films was demonstrated using pulsed laser deposition. Determining the effects of differing nanostructures on optical properties can lead to improvements in certain biomedical applications.

TABLE OF CONTENTS

LIST OF TABLES

LIST OF FIGURES

INTRODUCTION

X-ray Imaging

Computed radiography (CR), digital radiography (DR), and screen-film radiography are three different types of imaging modalities that are used in medical imaging to produce radiographs. An overview of these three modalities is shown in Figure 1. The traditional screen-film methods of producing x-ray images are largely outdated, and researchers have primarily focused on improving the modalities of computed and digital radiography since the late 1990s [1]. The screen-film method boasts advantageous characteristics such as simplicity and high information density, but these were overshadowed by the digital revolution and the ability of computed and digital radiography to produce digital images [2]. When compared to its analog counterpart, a digital x-ray image allows for easier storage, transport, and image data manipulation. Aside from integral digitalized images, computed and digital radiography outperforms screen-film methods in increased dose efficiency, a larger dynamic range, and the ability to reduce x-ray dose to the patient [3].

Digital radiography can be classified as either direct or indirect conversion, with multiple ways to achieve both. Direct conversion DR converts x-rays into electrical charges by using a photoconductor. Indirect conversion DR converts x-rays to visible light through a down-photon energy converting scintillator that is then quantified by a charge-coupled device or a thin film transistor array. Scintillators used for indirect conversion typically consist of Gd_2O_2S or CsI crystals in a polymer binder material [4]. Both indirect and direct conversation radiography develops an instantaneous digital radiograph.

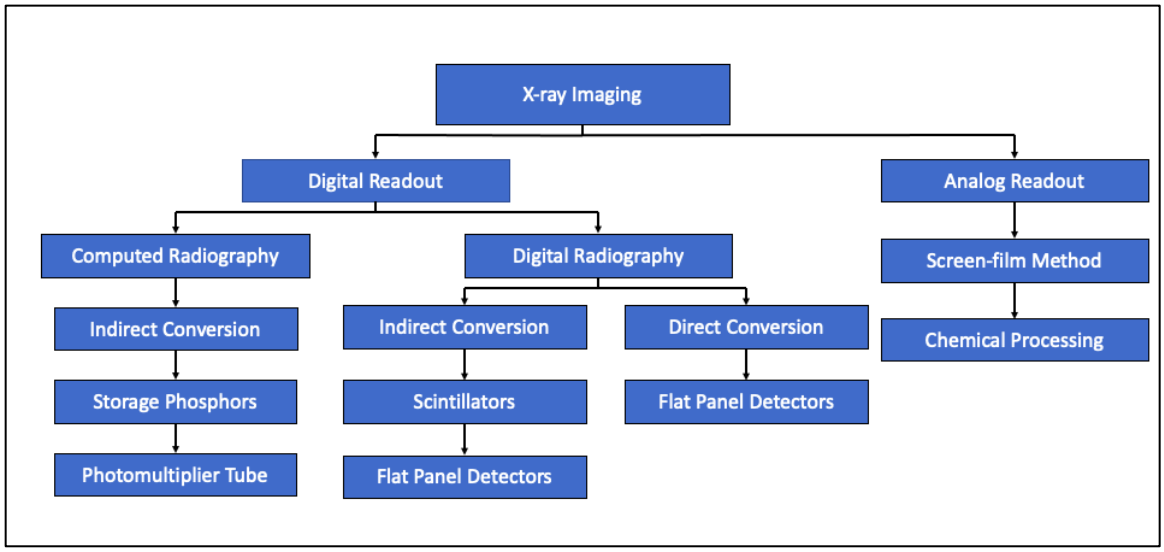

Figure 1. Overview of various types of x-ray imaging.

Computed radiography is characterized as an indirect conversion technique and uses an imaging plate containing storage phosphors. The image is acquired in a two-step process that is comprised of an exposure phase and a read-out phase. First, the imaging plate is placed in a light-tight enclosure and placed behind the object that is to be imaged for the exposure phase. Following exposure, the read-out is achieved by raster scanning of the imaging plate with a stimulating laser to trigger a process called photostimulated luminescence (PSL) [5]. A photomultiplier tube is used to quantify the PSL signal pixel-by-pixel to form the x-ray image. An illustration of the workflow of computed radiography is shown in Figure 2. The material in a CR imaging plate typically consists of $BaFBr:Eu^{2+}$ (BFB) storage phosphors in a polymer binder material. BFB storage phosphors can hold a latent image for over 8 hours and can be optically bleached and used again [6]. When compared to its digital counterpart, the passive read-out plates used in CR allow for easier positioning and set-up when compared to a DR plate that must be connected to a computer. Another advantage of CR over DR is the cost of implementation and maintenance.

Although PSL has been extensively researched and many storage phosphor materials have been developed and compared to the traditional BFB, a detailed mechanism of PSL is complex and controversial [7]. When a material capable of storage phosphor characteristics is exposed to x-ray radiation, free charge carriers are trapped in electron and hole traps that are created due to impurities and lattice defects [8]. A large bandgap from the impurities and lattice defects results in a metastable state in which the free charge carrier remains in the trapped position. In the case of BFB, the trap is an F-center with the bromine F-center being the only one to contribute to photostimulability [9]. An electron trapped in the bromine F-center transfers to Eu^{2+} complexes and not the conduction band when a stimulating laser is applied to the metastable state, resulting in PSL [10].

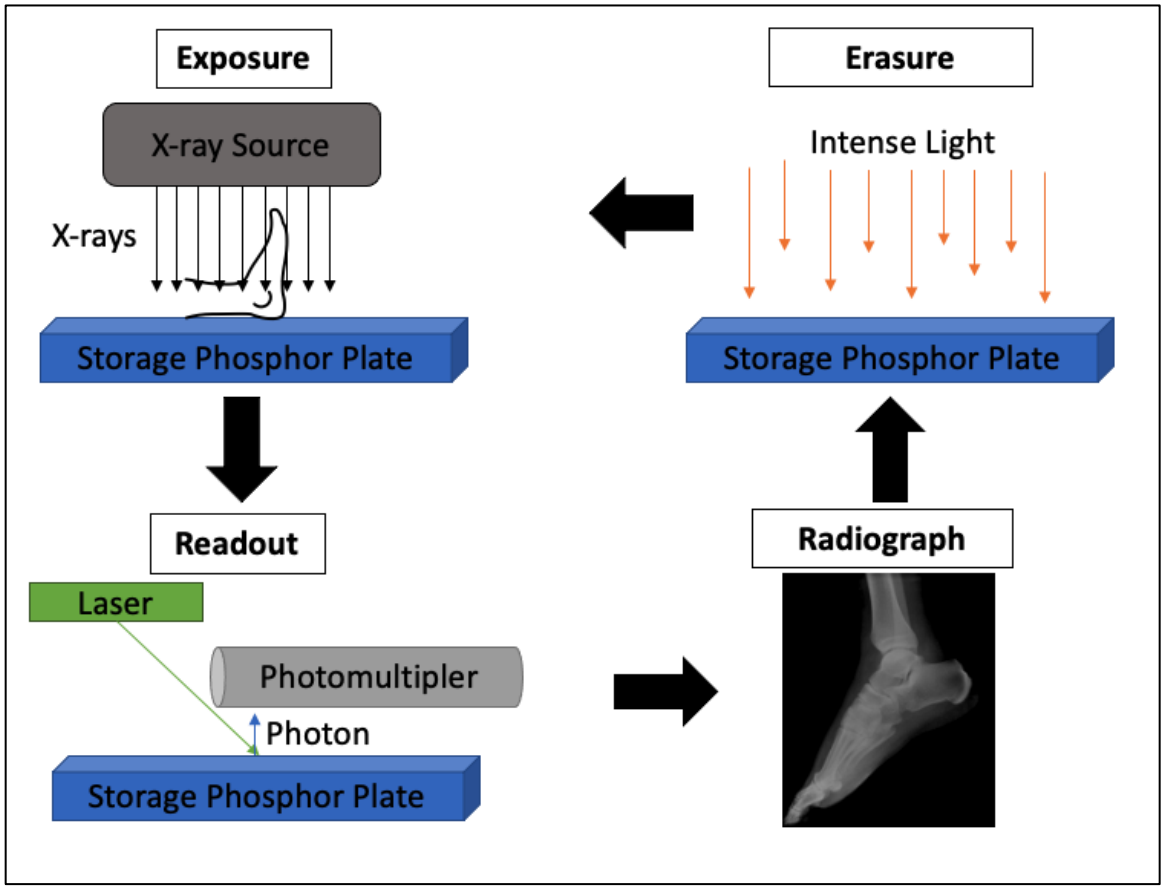

Figure 2. The process of computed radiography.

Many different experimental storage phosphor plates have been developed in an attempt to compete with the spatial resolution and conversion efficiency of commercial BFB plates. The spatial resolution of commercial plates is limited due to crystalline grain boundaries which causes scattering of the stimulating laser beam during the readout step, as illustrated in Figure 3(a). A storage phosphor plate transparent to the stimulating laser beam mitigates the chances of scattering (Figure 3(b)) and allows for images with increased spatial resolution. Although superior spatial resolution has been accomplished, the conversion efficiency of transparent plates is less than that of commercial BFB plates [11].

Light-Emitting Diodes

A light-emitting diode (LED) is a semiconductor device comprised of a P-N junction (a hole current and an electron current) and a phosphor layer. When a current is applied to the P-N junction, electrons are transferred from the N-type portion to an active region and holes are transferred from the P-type portion to an active region. During this transition, electrons transfer through an energy bandgap, and a photon is emitted. The energy of the emitted photon is largely dependent on the type of semiconductor device, or LED chip, and can result in an emission from the ultraviolet to infrared [12]. A phosphor layer can be applied to the transparent covering of the LED chip to provide additional tunability to the emission by using the up- or down-conversion process. An illustration of the basic make-up of an LED is shown in Figure 4.

LEDs are often referred to as solid-state lighting when they are employed in applications traditionally served by incandescent and fluorescent light sources. These applications include general indoor lighting, streetlights, automotive lights, and backlights in digital displays. Initially, LEDs were used as indicator lights and displays and were not considered as solid-state lighting until the early 2000s, when their energy-saving potential was recognized [13]. It was determined that the assimilation to solid-state lighting would decrease the electrical power used by lighting by more than 50% [14]. Another potential

benefit of more widespread use of LED solid-state light sources includes reduced emission of greenhouse gases as a byproduct of less energy consumption [15, 16].

The focus of the LED industry is solid-state light, but the developing technology has been influential to human health and many different biomedical applications [17]. The most widely studied effect of lighting on human health pertains to its impact on the human circadian rhythm, in which receiving sufficient biologically active light benefits an individual's well-being and productivity [18]. LED technology can also be beneficial to medical imaging, photobiomodulations, and optogenetics. With a simultaneous multiplane imaging technique, the ability of LEDs to produce a narrow band emission can be used to capture images at different depths. This is demonstrated in work conducted by Orsinger et al., in which a holographic image of ovarian cancer was reconstructed [19]. The same narrow band characteristics are used in narrow-band imaging to produce images with good contrast in capillaries and identify areas of increased vasculature [20]. Although traditional photobiomodulation treatment utilizes inert gas and semiconducting lasers, LEDs are quickly becoming a safer and more feasible alternative. LED photobiomodulation provides a safe treatment option with no side effects for a variety of different clinical applications, as shown in Figure 5 [21].

Pulsed Laser Deposition

Pulsed laser deposition (PLD) is a thin film synthesis technique that uses high energy photons to create a directional plume of target material that is collected on a substrate. The high energy photons are applied via laser pulses to avoid melting of the target material and lessen the chances of a laser-plume interaction. The laser beam is typically focused on a target at a 45° angle of incidence. When the laser ablates the target, a transient plume is developed, comprised of many different species of the target material. The plume can be comprised of electrons, ions, neutral atoms, atom clusters, micron size particulates, and molten droplets [22]. The plume materials expand rapidly away from the target, with the densest portion of the plume ejected at a 90° angle relative to the target. A schematic of a

PLD apparatus is shown in Figure 6. A traditional PLD apparatus uses a UV excimer laser and a substrate that is largely dependent on the desired application of the thin film. Figure 7 shows an image of the PLD apparatus in the Center for Laser Applications at the University of Tennessee Space Institute.

When compared to other thin-film synthesis techniques, PLD is unique in its capability for stoichiometric transfer from target to substrate, the vast number of materials that can be used as a target, ease of film thickness control, and the ability to make multilayer films [23]. The technique is historically known for developing superconducting thin films but has been used for a large variety of applications. Some of these applications include electrical circuit components, optical materials, and coatings for medical applications [24].

Summary of Work

This work details the use of PLD to produce optically active rare-earth doped films that can be used for biomedical applications. Chapter I focuses on the development of an Eu-doped $BaCl_2$ glass-ceramic storage phosphor film by exploring different glass matrix materials and evaluating their performance for computed radiography applications. Chapter II investigates different nanolayered configurations in an Eu-doped BaF_2/Al_2O_3 thin film and determines their suitability to be used as a phosphor material in UV-pumped white-light LEDs. Chapter III explores the optical effects of adding a Mn dopant to the films developed in Chapter II.

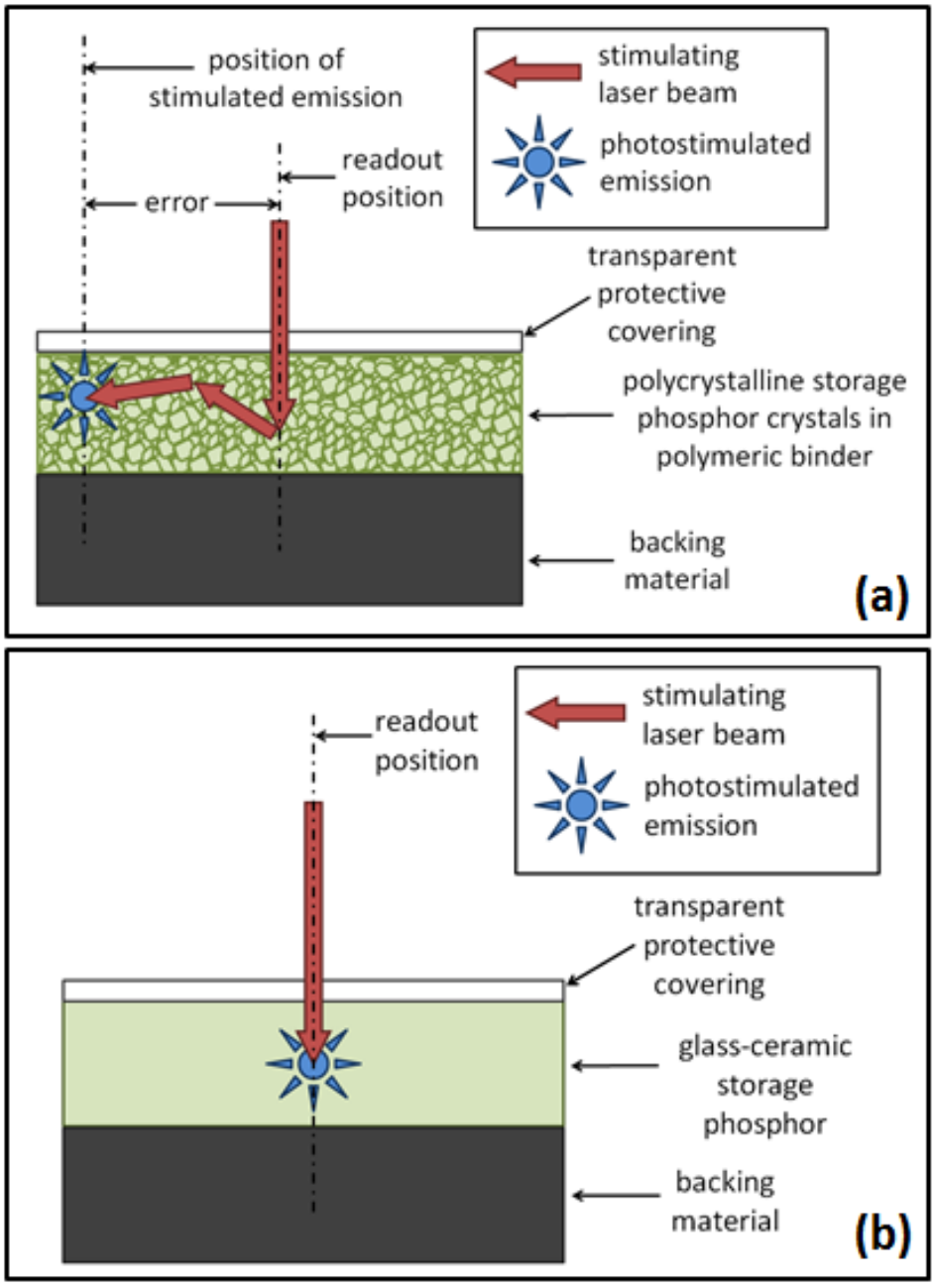

Figure 3. (a) Scattering of the stimulating laser beam at the grain boundaries of a polycrystalline storage phosphor causing a decrease in spatial resolution and (b) reduced scattering in a glass-ceramic storage phosphor for improved spatial resolution. [12]. Used with permission.

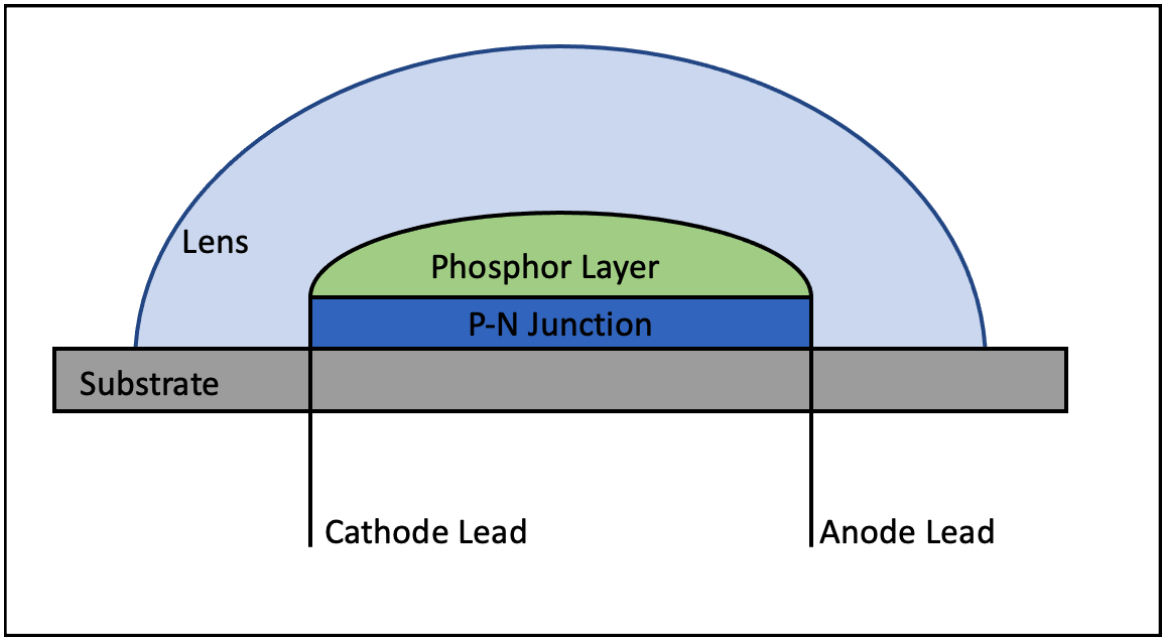

Figure 4. Basic schematic of a light-emitting diode.

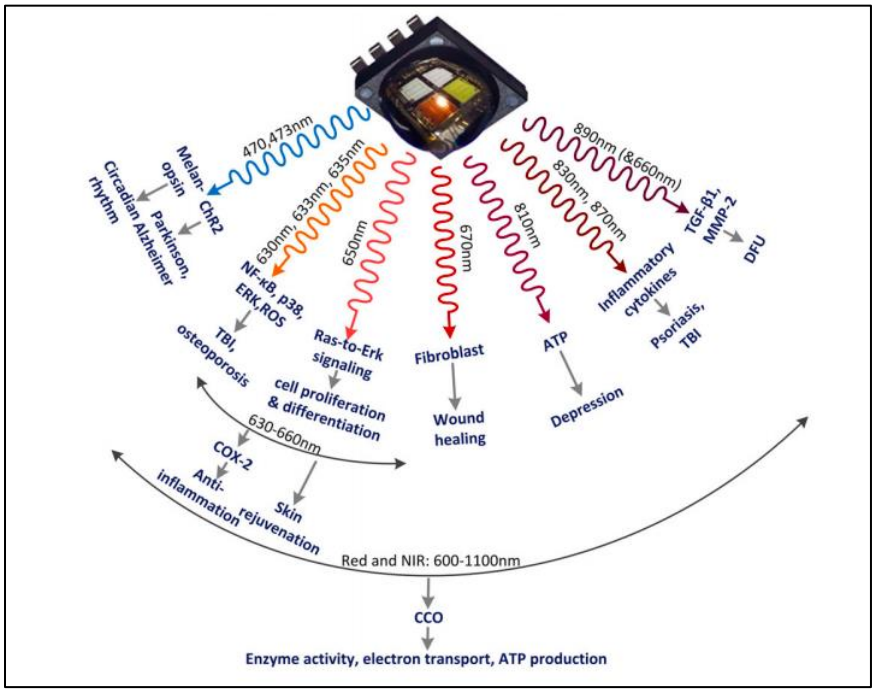

Figure 5. LEDs with different wavelengths and corresponding biomedical applications. Used with permission [17].

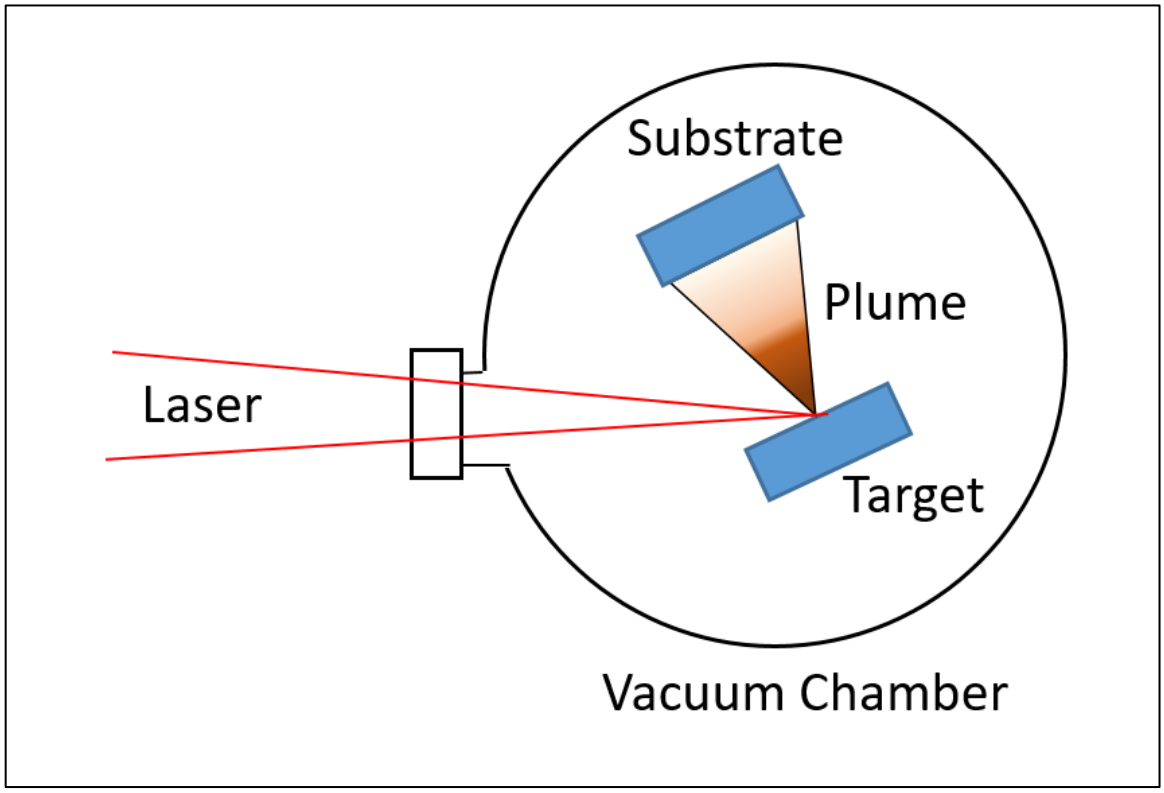

Figure 6. Schematic of pulsed laser deposition apparatus.

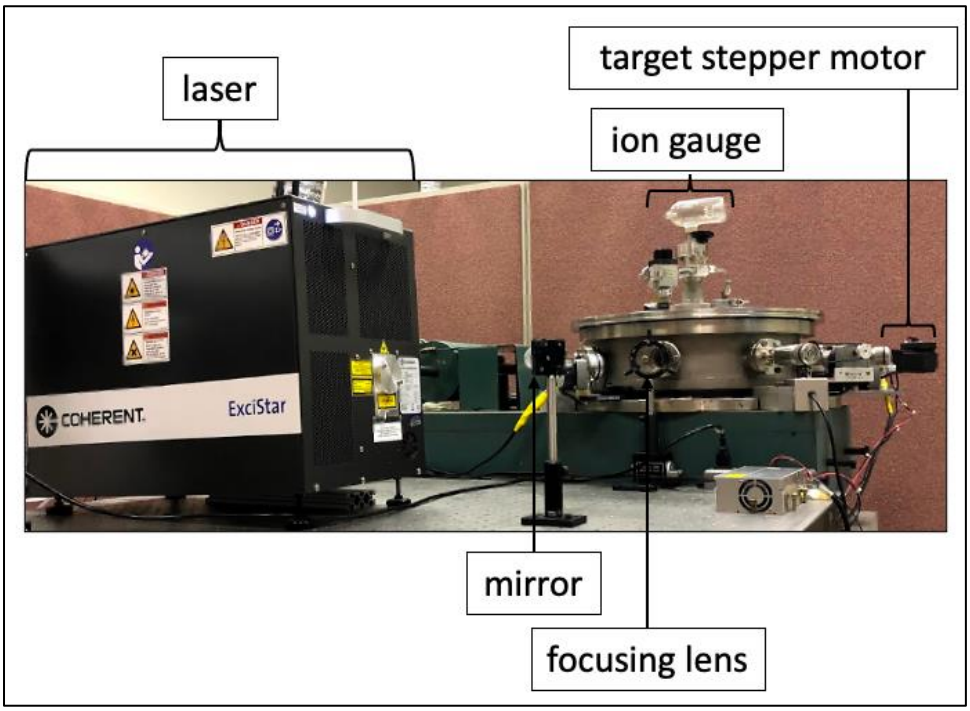

Figure 7. Pulsed laser deposition apparatus at UTSI.

CHAPTER I

EUROPIUM-DOPED BARIUM CHLORIDE STORAGE PHOSPHOR PLATE SYNTHESIZED BY PULSED LASER DEPOSITION

A version of this chapter was originally published by C.W. Bond, Y. Jin, J.C. McDearman, A.F. Howansky, R.L. Leonard, A.R. Lubinsky, A.K.Petford-Long, and J.A. Johnson:

Bond CW, Jin Y, McDearman JC, et al. Europium-doped barium chloride storage phosphor plate synthesized by pulsed laser deposition. J Am Ceram Soc. 2021;00:1–9. doi.org/10.1111/jace.17775

C.W. Bond was responsible for all writing and research activities in the original article except as noted: Y. Jin provided the SEM images. J.C. McDearman assisted with sample synthesis. A.F. Howansky and A.R. Lubinsky conducted PSL measurements. J.A. Johnson, A.K. Petford-Long, and R.L. Leonard provided overall guidance.

Abstract

In computed radiography, scattering of the stimulation light by the storage phosphor crystals in the imaging plates negatively impacts spatial resolution. Storage phosphor plates with thinner phosphor layers have been developed to reduce scattering distance and increase spatial resolution, although at the expense of reduced x-ray absorption. The authors hypothesize that a transparent or translucent nanostructured film, containing a much higher percentage of storage phosphor crystals than achievable in bulk glass-ceramic materials made by conventional methods, may have acceptable photostimulated luminescence efficiency and imaging performance characteristics greater than commercial imaging plates. Films have been produced via pulsed laser deposition by alternating target materials of the storage phosphor $BaCl_2:Eu^{2+}$ and either silica or silicon. X-ray diffraction and photoluminescence characterization were conducted to confirm the presence of $BaCl_2:Eu^{2+}$ crystallites. The films were able to store optical data and be read out to produce x-ray radiographs demonstrating 50 μm spatial resolution. The performance of the experimental storage phosphor plates was compared to commercially-available imaging plates. The authors demonstrate for the first time the synthesis of a glass-ceramic imaging plate for computed radiography by pulsed laser deposition.

Introduction

Optical data storage utilizes photons and electron trapping materials (ETM) to read and write information in applications such as radiography [25] and, more recently, big data storage [26, 27]. An irradiation light source is used to create electron-hole pairs within the ETM, followed by sequential recombination of the electron holes that release photons resulting in the rendering of the stored data through photostimulated luminescence (PSL). The electron-hole recombination is typically facilitated by an excitation laser in radiography or by heating for thermally stimulated luminescence in high-capacity storage systems [28-30]. Depending on the application, the importance of particular ETM characteristics will vary. With regards to medical imaging, adequate detective quantum efficiency (DQE) and modulation transfer function (MTF) are necessary to render quality radiographs [31, 32].

Computed radiography (CR) is a type of digital x-ray imaging technique that is used for medical imaging and nondestructive testing, where the ETM is referred to as a storage phosphor plate. The advantages of CR over other digital x-ray imaging modalities include its inexpensive implementation, ease of image plate placement, and dynamic range with a linear trend to X-ray exposure over four orders of magnitude [33, 34]. $BaFBr:Eu^{2+}$ (BFB) is the most common commercially-used storage phosphor plate, followed by $BaFI:Eu^{2+}$ [35, 36]. These crystalline materials are held together by an organic binder as powder plates, with particle size ranging up to 40 μm [37]. The primary limiting factor to spatial resolution in CR radiographs, which typically ranges from 10 – 20.0 lp/mm, is scattering of the stimulation light in the turbid phosphor layer [38].

Due to their ability to host small optically-active crystallites in a transparent amorphous matrix, rare-earth doped glass ceramics have been considered as an alternative storage phosphor plate material for high spatial resolution radiographs [39]. Fluorochlorozirconate (FCZ)-based glass ceramics utilizing europium-doped barium chloride nanocrystals in the orthorhombic phase [40] have been a popular material for radiographs recorded with CR.

Experimental storage phosphor plates using barium chloride single crystals with a cerium rare-earth dopant, and lithium borate glass matrices with a europium dopant have also been developed [41-43]. When compared to commercially available BFB plates, FCZ storage phosphor plates have demonstrated high spatial resolution of 13 lp/mm, but with a 20% diminished relative PSL intensity [44, 45].

FCZ storage phosphor plates are initially synthesized as an amorphous material, and subsequent thermal annealing precipitates doped nanocrystals within the glass matrix, providing the optically-active luminescent centers [11, 46]. When more luminescent centers are introduced into the glass matrix, via more crystalline material or increased thermal treatment, aggregation of the crystallites becomes an issue [39, 47]. The aggregation results in diminished spatial resolution due to light scattering caused by increased crystalline size [40].

The goal of this study is to demonstrate a scalable synthesis option to produce storage phosphor plates with superior spatial resolution, coupled with comparable relative DQE intensity, by producing a nanostructured transparent glass-ceramic storage phosphor plate via pulsed laser deposition (PLD). The films contain small nanocrystals isolated by a surrounding amorphous matrix. Experimental thin films produced by this physical vapor deposition technique lack the amount of material found in commercially available or experimental bulk storage phosphor plates, but conclusions can be made by comparing a material ratio to optical performance. PLD has been used to produce films with a thickness of over 100 μm for alternate applications [48, 49]. With an automated synthesis process, this novel technique could be applied to produce samples with comparable thickness and amount of material as its commercial counterpart.

A piece of sintered, doped barium chloride and a glass matrix material were affixed to an aluminum disk to create a multicomponent PLD target. Fused silica and silicon wafers were used as PLD targets for the glass matrix materials. Alternating target materials were ablated with a laser so that the glass matrix will isolate the crystalline material. This constrains the

crystallites to a size much smaller than the wavelengths of visible light, allowing the samples to retain their transparent properties. The samples' structural characteristics were determined by x-ray diffraction (XRD) and scanning electron microscopy (SEM) analysis and the luminescent properties were determined by phosphorimetry. The PSL intensity of the experimental storage phosphor plates was compared to that of commercially available BFB. A radiograph of a test phantom was produced, allowing determination of achievable spatial resolution.

Materials and Methods

Films were grown on four 25 x 25 mm substrates concurrently: three fused silica substrates and one silicon substrate were coated during each deposition procedure. The fused silica substrates were cut from a UV Grade Corning 7980 500 µm thick wafer and the silicon substrates were single-side polished test grade 475-575 µm thick wafers with <100> crystal orientation. Prior to film growth, the substrates were cleaned ultrasonically in high purity acetone for ten minutes, followed by ten minutes in high purity methanol. After the ultrasonic cleaning, the fused silica substrates were soaked in piranha solution (1:1 volume ratio of 93% H_2SO_4 and 35% H_2O_2) for two minutes, then soaked in ultrapure water for 1 minute and dried with compressed argon. Following ultrasonic cleaning, the silicon substrates were soaked in a buffered oxide etch solution (6:1 volume ratio of 40% NH_4F in water to 49% HF in water) for 20 seconds, and then rinsed with ultrapure water and dried with compressed argon. The mounting hardware used to affix the substrate to the sample holder creates masked areas, i.e., regions without film on the substrate.

Three different materials were used for PLD targets: fused silica, silicon, and europium-doped barium chloride. The silica and silicon specifications and cleaning procedures are identical to the aforementioned substrates. The europium-doped barium chloride target was synthesized in an argon atmosphere glovebox with an attached tube furnace. The barium chloride was doped with 1% europium (II) chloride, with a total sample mixture weight of 10 g used for the melt. Initially, the $BaCl_2$ powder was dried in a platinum crucible for 10

minutes at 300 °C. Following the drying, $EuCl_2$ was added to the crucible and mixed thoroughly. The crucible was then placed back in the furnace and heated to 1000 °C at a rate of 5 K/min. The sample was held at 1000 °C for 30 minutes before cooling to 25 °C at a rate of 1 K/min. The sample was removed from the crucible and polished before being fixed to an aluminum holder along with the respective host material target, illustrated in Figure 8. The target had an approximate diameter of 35 mm and thickness of 3 mm. A new $BaCl_2:Eu^{2+}$ target was synthesized for each sample.

Samples were synthesized via pulsed laser deposition using an ArF excimer laser (ExciStar, Coherent Inc) with a wavelength of 193 nm. A 200 Hz repetition rate was used with a rated pulsed length of 15 ns. The computer-controlled laser energy was set to 5.0 mJ, which equates to a laser fluence of 8.3 J/cm^2 based on a 0.06 mm^2 spot size. All samples were synthesized under vacuum with the background chamber pressure remaining below 3.0 x 10^{-6} Torr. During depositions, the substrate temperature remained below 27 °C. The targets were fixed to the holder with rotational movement controlled by a stepper motor (Nema 23 Integrated StepSERVO, Applied Motion Products). Two samples were made with different host materials (fused silica or silicon) and a $BaCl_2:Eu^{2+}$ target. The matrix was deposited first using 1000 laser pulses on the respective host, followed by 5000 laser pulses on the $BaCl_2:Eu^{2+}$. This bilayer was repeated for a total of 500 cycles and then capped with a final 1000 laser pulses on the glass matrix target material. The final deposition of the glass matrix target material is intended to be a protective layer to prevent oxidation of the sample.

The thickness was characterized with stylus profilometry (Dektak 150, Veeco). The 12.5 µm diamond tip stylus traveled from one masked portion of the substrate to another with a force of 6.50 mg, revealing the step height. The length of the scan was 500 µm with a duration of 120 seconds resulting in a resolution of 0.014 µm/sample. The masked portion was used as the reference and the plateau was averaged to determine an average step height and average roughness.

Scanning electron microscopy (SEM) (Nova 600 NanoLab, FEI) was used to characterize the surface morphology and the cross-section structure of the film sample. To obtain the cross-section of the film, the sample was cleaved from the back side of the substrate by using a diamond scribe and cleaving pliers. Then the sample was mounted on an SEM holder with the cross-section of the sample facing upwards for characterization.

A Philips X'Pert MRD X-ray Diffractometer (PANalytical Inc) with a Cu anode x-ray source and a PW 3011/10 detector was used for x-ray diffraction measurements. Scans were conducted over a 2θ range of 20 ° to 80 ° with a step size of 0.05 ° and a dwell time of 10 s at each angle.

The photoluminescence of the samples was characterized by a PTI QM30 model 810/840 phosphorescence/fluorescence spectrofluorometer. The PTI Felix32 software was used to collect the excitation and emission spectra. The scans used a 1 nm step size, 50 μs integration time, and a 100 Hz lamp frequency. The resultant data is the average of three subsequent scans and a background acquired prior to the measurements. The excitation scan ranged from 225 to 390 nm with an emission wavelength of 400 nm. The emission scan ranged from 310 to 525 nm with an excitation wavelength of 310 nm.

The ability of the films to store optical data was determined by measuring photostimulated luminescence using a 532 nm pumped diode Nd/YAG laser (Compass 215M, Coherent Inc) and a 4-inch integrating sphere with ports for the sample and for a photomultiplier tube module. A shutter controlled the stimulating laser light, and the photostimulated emission was collected by the integrating sphere and directed to the photomultiplier tube, where 2 colored bandpass filters block the laser light and pass the photostimulated light. The photostimulation signal *vs.* time was recorded by a digital storage oscilloscope (TDS 2024B, Tektronix). Before photostimulation, the samples were exposed to x-rays using an x-ray tube with a tungsten anode at 70 kVp. A comparison commercial sample was exposed for 320 msec at 10 mA, and with 20 mm of Al filtration, producing 27.7 mR of x-ray

exposure at the sample. The experimental samples were exposed for 1.25 sec at 400 mA, producing 80 R of x-ray exposure at the sample.

To compare the photostimulated luminescence output, an exponential decay curve was fitted to the voltage data of the two experimental samples and a BFB commercial sample. The data was fitted using the CFTool in MATLAB to the following equation:

$$I(t) = I_0 e^{-\lambda t} \tag{1}$$

The initial signal intensity is I_0 and the stimulation speed is λ. The stimulation speed is a measure of how fast stored data can be retrieved from the phosphor plate. Because the PSL signal of samples lasted approximately 8 seconds, the following definite integral was performed for quantitative comparison:

$$PSL\ Area = \int_0^8 I(t)dt \tag{2}$$

The values were determined both mathematically and graphically across a range of 800 points. The absorbed x-ray energy was determined separately for each experimental sample and for the commercial sample. The x-ray fluence per units of exposure was determined by the following equation [50]:

$$\xi(E) = \frac{5.34 \times 10^5}{E(\frac{\mu_{en}(E)}{\rho})_{air}} \tag{3}$$

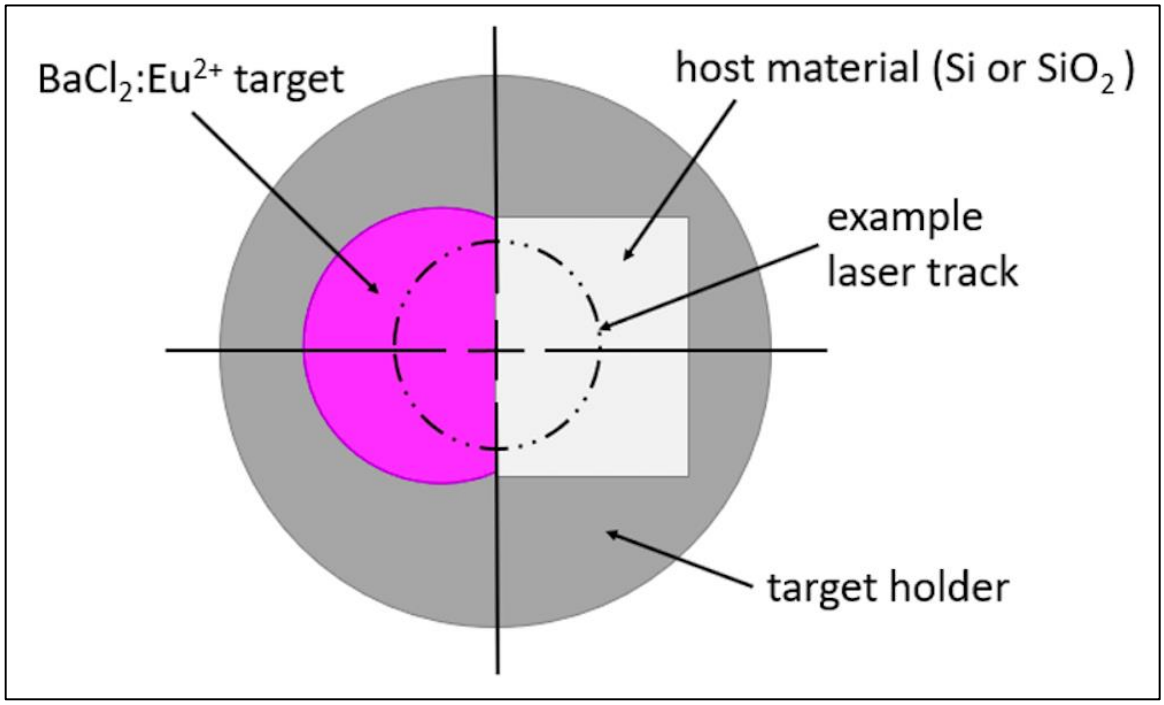

Figure 8. Illustration of multi-component target showing a europium-doped barium chloride puck and a host material fixed to a target holder.

The energy of the x-ray in units of keV is E and the mass energy absorption coefficient for air in units of cm^2/g is μ_{en}/ρ. An estimated 10:1 molar ratio of $BaCl_2:Eu^{2+}$ (1% $EuCl_2$) to host matrix (Si or SiO_2) and a 3.8 g/cm^3 density was used to calculate the x-ray mass attenuation coefficients for the experimental samples. The coefficients were calculated based on a 50:50 molar ratio $BaF_2:BaBr_2$ mixture and a 4.8 g/cm^3 density for the commercial BFB sample.

For x-ray imaging, the sample was exposed to a copper anode x-ray tube with a wavelength of 1.54 Å operating at 45 kVp and 40 mA. The sample was exposed for 10 minutes and the readout was conducted 5 minutes after exposure. A line-pair phantom with a lead thickness of 0.03 mm and a resolution range of 1.5 – 20.0 lp/mm was placed on top of the storage phosphor plate during exposure. Image readout was obtained with a computed radiography scanning apparatus similar to the one detailed in Lubinsky *et al.* [51].

Results and Discussion

Visual Characterization

One of the as-made europium-doped barium chloride targets is shown illuminated with visible light in Figure 9(a). Visual observation of the target under a 254 nm UV lamp was conducted to ensure the europium was distributed in the crystalline $BaCl_2$ during synthesis. As seen in Figure 9(b), the target exhibited a violet emission when excited by the UV lamp, which is characteristic of $BaCl_2:Eu^{2+}$ emission.

The two sample types were visually similar, being translucent with a slight white coloration. A sample composed of $BaCl_2$, Eu, and SiO_2 is shown in Figure 10(a), with half circles visible on the edges of the substrate due to masking during sample growth. The sample retained the characteristic $BaCl_2:Eu^{2+}$ emission that was seen by the target when excited by UV light, shown in Figure 10(b). The sample with a silicon matrix had a thickness of 12.70 µm with an average roughness of 4.49 µm while the fused silica matrix had a thickness of 12.71 µm with an average roughness of 12.76 µm. Although the sample

containing the silicon matrix was smoother, both samples were much rougher than expected, which was undesirable for achieving a nanostructured sample. An explanation for the unexpected roughness is provided in the results section of the SEM characterization. The films demonstrated adequate adhesion to the substrate with no delamination occurring during initial characterization.

SEM analysis validated the thickness measurements determined by profilometry. A top-view SEM image of the film with a Si matrix is shown in Figure 11(a). The surface of the film is made up of mostly spherical particulates with a size range of 1–4 μm. The particulates are responsible for the rough topography of the films as well as for their translucent, cloudy appearance. Cross-section SEM analysis revealed voids throughout the sample due to the variation in size of the particulates within the film. A cross-section SEM image is shown in Figure 11(b) with an inset of a high magnification SEM image highlighting the voids within the film. After the sample was exposed to the atmosphere for approximately 1 hour, delamination of the film from the silica substrate occurred. The delamination suggests that the protective capping layer of the glass matrix was not continuous and allowed moisture penetration. Due to the hygroscopic nature of $BaCl_2$, the moisture penetration resulted in structural changes, causing the film adhesion to fail under ambient conditions.

The authors hypothesize that the abundance of particulates within the sample is the result of $BaCl_2$:Eu^{2+} target degradation. Although the target was polished prior to ablation, its surface appeared rough after the deposition process was completed. Multiple laser passes on the target were required due to the relatively large amount of material necessary to synthesize a functional imaging plate. Ablation of the roughened surface on subsequent passes may have led to the ejection of large particulates, which negatively affected layered growth. The authors speculate a more transparent film with fewer particulates could be synthesized by using a lower laser fluence and more frequent target polishing. A technique that will be used in future work is positioning the substrate off-axis with respect to the target, which results in a film with fewer particulates.

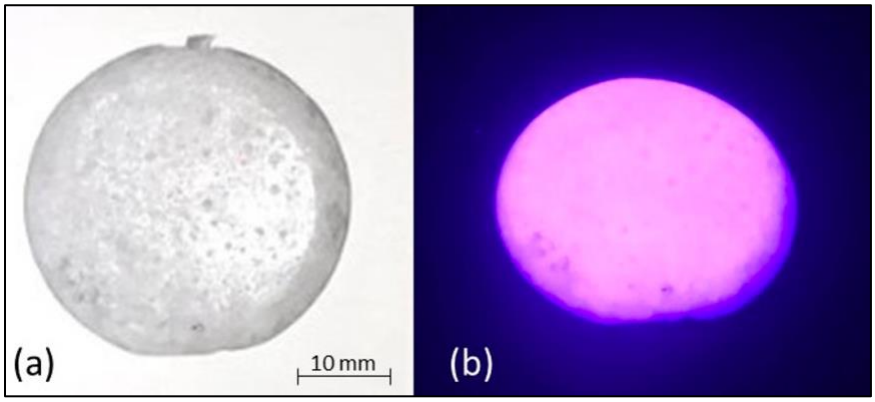

Figure 9. As-made $BaCl_2:Eu^{2+}$ pulsed laser deposition target in (a) visible light and (b) excited by a 254 nm UV light exhibiting violet emission.

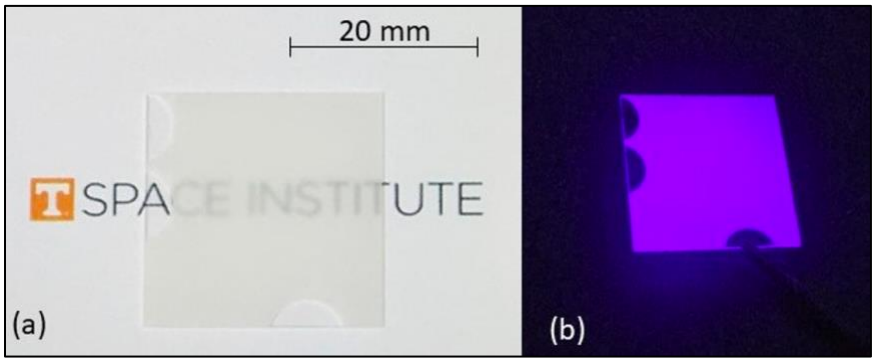

Figure 10. Sample composed of $BaCl_2$, Eu, and SiO_2 in (a) visible light and (b) excited by a 254 nm UV light exhibiting violet emission.

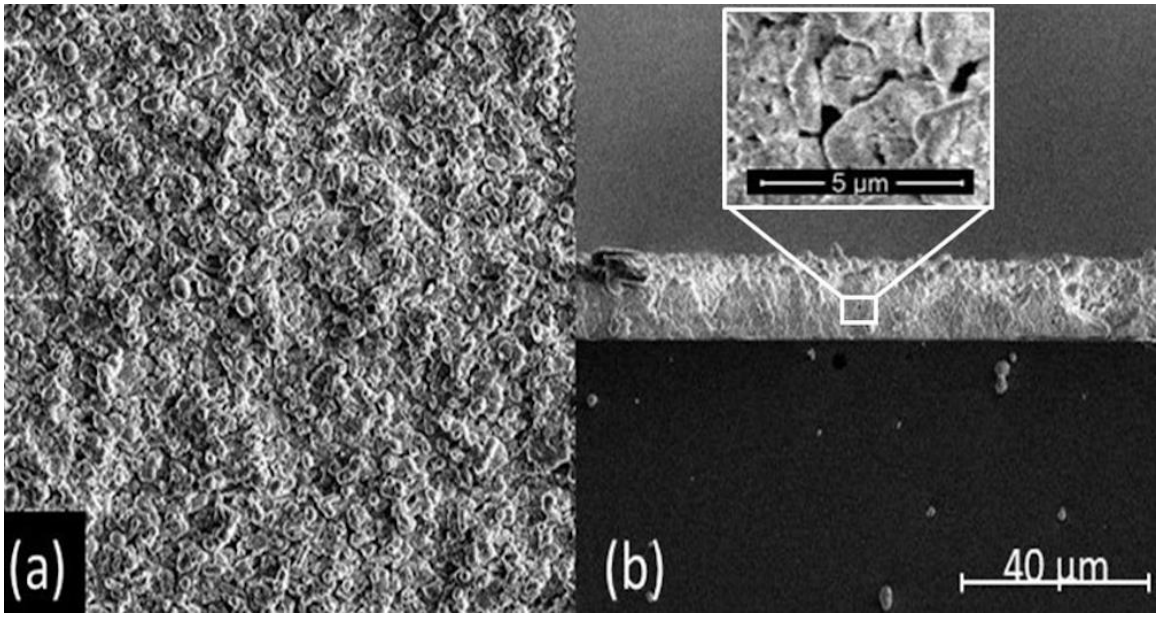

Figure 11. SEM (a) top view and (b) cross-section images of experimental $BaCl_2$ film with a Si matrix. A higher magnification image revealing voids in the film is included as an inset. The top view reveals mostly spherical particles on the surface.

X-ray Diffraction

The X-ray diffraction data for the two experimental samples is shown in Figure 12 along with calculated x-ray diffraction patterns for orthorhombic barium chloride (ICSD 16915), hexagonal barium chloride (ICSD 2190), and cubic silicon (ICSD 51688). Both samples exhibited observed peaks at 21.0, 22.0, 23.9, 31.0, 38.1, and 39.3 ^{o} 2θ which is indicative of orthorhombic phase $BaCl_2$ crystallites. There is a possibility of hexagonal phase $BaCl_2$ in both films, which accounts for the small observed peaks at 32.0 ^{o} 2θ. Barium chloride predominately forms in the orthorhombic phase over the unstable hexagonal phase, but a small amount of hexagonal $BaCl_2$ cannot be excluded [52]. The peaks in the X-ray diffraction pattern are broad, likely as a result of the small crystallite size in the $BaCl_2$ layer, but also as a result of crystalline disorder within the nanocrystals. No crystalline silicon was detected in the Si matrix sample, indicating that the silicon was deposited as an amorphous material. A broad amorphous peak is shown in the data that can be attributed to the matrix materials within the sample. The peak observed at 26.6 ^{o} 2θ is attributed to an unknown phase, which has previously been documented in the literature [32, 44, 53]. Peaks observed at 35.2 and 43.7 ^{o} 2θ are indicative of aluminum and can be attributed to the sample stage.

Optical characterization

The emission spectra for the ablation target and the two films are shown in Figure 13. All spectra display a broad emission peak associated with the $4f^6 5d^1$ to $4f^7$ emission of Eu^{2+} [54]. However, the emission peaks of the films are blue shifted and slightly broader than that of the target, which can be explained by differences in the crystal field. Wang et al. proposed that different intrinsic stresses can weaken the Eu^{2+} crystal field splitting due to effects of neighboring cations and result in a blue-shifted emission [55]. The 5d electron transition for Eu^{2+} occurs in the outer orbitals, which allows the atomic coordination in the surrounding $BaCl_2$ host to influence the transition [56]. Due to the deposition process, the $BaCl_2$:Eu^{2+} crystallites in the two films are likely more crystallographically disordered than

the $BaCl_2$ in the target, leading to a decreased crystal field and the blue shifting and broadening of the spectra. The formation of disordered crystalline phases as a consequence of PLD synthesis is detailed in work conducted by Bendersky *et al.* [57]. Additionally, for the thin films, the SiO_2 and Si amorphous matrices may influence the crystal field at their interface with the $BaCl_2:Eu^{2+}$ crystallite surfaces, leading to additional differences in the spectra; the effects, however, would likely not be very pronounced, as they apply only to the surface of the crystallites and not the entirety of their volume. Peak analysis by deconvolution did not yield further insight into the source of the shifting and broadening of the peaks or their asymmetrical nature.

Computed Radiography

The PSL curve fits for the experimental storage phosphor plates are shown in Figure 14, along with an inset of the fit curve of a commercial plate for reference. It should be noted that the experimental samples and the commercial sample did not receive the same dosage of x-ray exposure, but differences in the absorbed x-ray energy have been accounted for in the comparison. The PSL area values, absorbed energies, and conversion efficiencies (CE) along with the CE ratio relative to the commercial plate are shown in Table 1.

The BFB commercial storage phosphor plate had a CE that is 1530 times higher than that of the experimental plate with a silica matrix and 4900 times higher than the experimental plate with a silicon matrix. The CE of both experimental plates is too low to be considered as a potential replacement to traditional BFB storage phosphor plates in dose-critical applications such as medical imaging. The sample with the silica matrix had a CE that is about three times higher than the sample with the silicon matrix, despite the much rougher surface. The authors hypothesize that SiO_2 provides a superior, more continuous, final protective layer, preventing degradation of the luminescent material, $BaCl_2:Eu^{2+}$, which is hygroscopic, resulting in a more efficient imaging plate. Some degradation was visually observed in both samples, however.

Using a line-pair phantom, it was determined that the images rendered from the experimental storage phosphor plate with an SiO_2 matrix could resolve 10 lp/mm, or a spatial resolution of 50 µm. The spatial resolutions of the experimental plates are comparable to most commercially-used storage phosphor plates and, depending on scanner specifications, can be considered high-resolution [58]. A radiograph of the line-pair phantom achieved from an experiment plate is shown in Figure 15.

Although the CE of the experimental plates was much less than that of the traditional BFB storage phosphor plate, the potential remains for the favorable spatial resolution of the experimental plate to be utilized in nondestructive testing applications, where dose is of lesser concern when compared to medical imaging. Nondestructive testing is often used to detect welding discontinuities and defects using longer exposures and higher energy photons. Further experimentation would need to be conducted, using increased exposure dose and imaging thicker materials, to evaluate the practicality of applications for the experimental films in nondestructive testing.

Future Work

Although the experimental plates are not practical in computed radiography applications, this synthesis technique could be applied to develop a scintillating film that can be incorporated into a flat panel detector for use in indirect digital radiography. PLD can be employed to synthesize a glass-ceramic film, with high scintillator to glass ratio, with the opportunity to utilize certain scintillating materials that may not be applicable with bulk glass ceramics synthesized via traditional methods.

Traditional indirect flat panel detectors (FPD) are typically comprised of an x-ray conversion screen of scintillating phosphors and a photodiode-thin film transistor (TFT) array deposited on a glass substrate that is not optically active. It is common, increasingly so in higher energy applications, for x-rays to pass through the conversion screen and the TFT array unattenuated, which can limit the performance of these devices. Developing an FPD with a sandwich of two x-ray conversion screens, in which the bottom screen is an

optically active glass-ceramic screen that serves a substrate for a bidirectional TFT array, has shown the potential to enhance the performance of these devices in work conducted by Leonard et al. [59]. The glass-ceramic substrate has the ability to capture previously unattenuated x-rays and convert them to visible light so that they may contribute to the radiograph. A schematic of an indirect flat panel detector with a scintillating glass-ceramic film is shown in Figure 16. The schematic shows an optional glass thin film on top of the scintillating film, which can be used to facilitate the incorporation of the TFT array.

A prototype has been developed using PLD, consisting of $BaCl_2:Eu^{2+}$, which serves as both luminescent and scattering centers, and a borosilicate glass top layer. Using an ArF excimer laser, 2.5×10^6 laser pulses were applied to a $BaCl_2:Eu^{2+}$ target, followed by 5.0×10^4 laser pulses on a borosilicate target. The resultant film is shown in visible light and luminescing when exposed to 45 keV x-rays in Figure 17. Although the $BaCl_2:Eu^{2+}$ film demonstrated the ability to use the synthesis technique for this application, further work needs to be conducted to investigate different luminescent materials to increase scintillation yield.

Conclusion

Translucent layered thin films composed of alternate layers of europium-doped barium chloride nanocrystals and an amorphous glass matrix were synthesized via pulsed laser deposition. XRD was conducted to confirm that orthorhombic phase $BaCl_2:Eu^{2+}$ crystallites were incorporated into the film. SEM results revealed that the desired nanostructured layered films were not achieved, which was hypothesized to be due to inclusion of large particulates caused by PLD target degradation. The silicon and silica-based films were similar in performance. The films exhibited a characteristic Eu^{2+} emission at 405 nm when excited by UV light. When the films storage phosphor capabilities were compared to a commercially available BFB plate, the conversion efficiency (CE) was approximately three orders of magnitude lower, even though the difference in amount of material and in x-ray attenuation were considered. However, for applications such as nondestructive testing, in which dose is not critical, the CE would be of lesser concern. The experimental storage phosphor plate was used to image a line-pair phantom through

computed radiography. The radiograph revealed a spatial resolution of 10 lp/mm, which is commercially considered to be high-resolution. The authors demonstrate for the first time the synthesis of a glass-ceramic imaging plate for computed radiography by pulsed laser deposition. This synthesis technique has the ability to develop scintillating glass-ceramic substrates that can be used in indirect FPD, but further material investigation must be conducted.

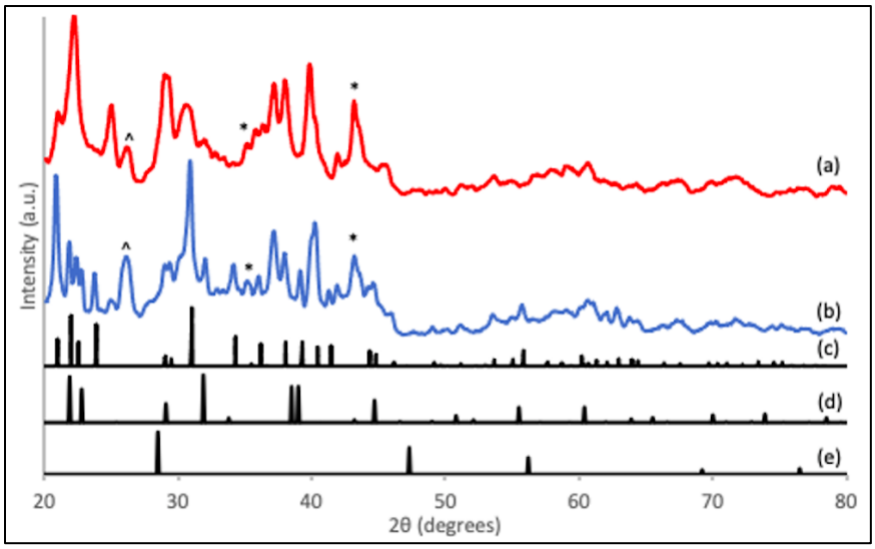

Figure 12. X-ray diffraction results for two samples with different targets used for host matrices: (a) film grown with SiO_2 target, (b) film grown with Si target, (c) orthorhombic phase $BaCl_2$ powder diffraction file (ICSD 16915), (d) hexagonal phase $BaCl_2$ powder.

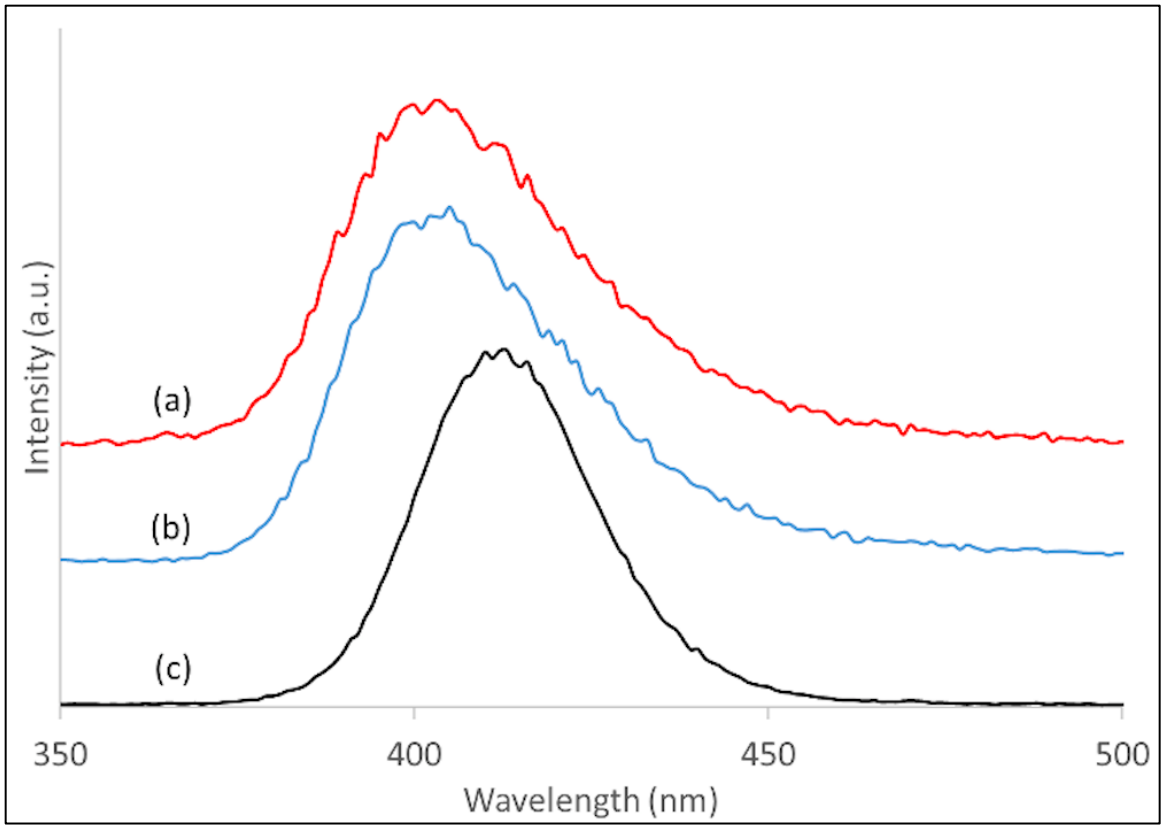

Figure 13. Normalized emission spectra of sample with (a) SiO_2 matrix, (b) Si matrix, and (c) material from the $BaCl_2:Eu^{2+}$ PLD target. All samples were excited at 310 nm. The emission of the experimental films exhibited a blue shift when compared to the target, which is attributed to increased crystalline disorder.

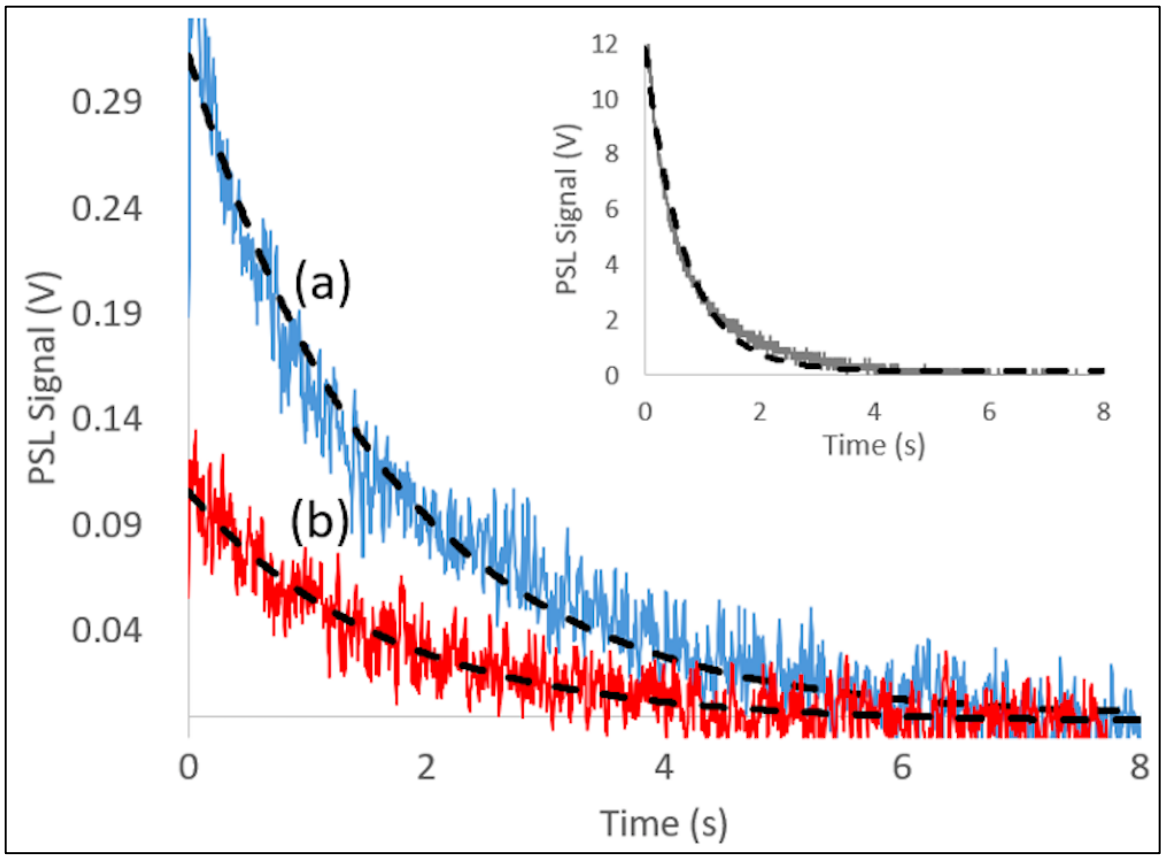

Figure 14. PSL decay curves for experiment storage phosphor plates with a (a) SiO_2 matrix and a (b) Si matrix. Exponential decay curve fits are shown with a dashed line. A PSL curve for a commercial BFB storage phosphor plate is included as an inset.

Table 1. Values from integrals of PSL decay curve fits along with data regarding to the amount of material.

Sample	*PSL Area*	*Absorbed Energy (keV/mm²)*	*Conversion Efficiency (PSL/Energy)*	*Ratio*
SiO_2 Matrix	0.517	1.02×10^{10}	5.05×10^{-11}	6.53×10^{-04}
Si Matrix	0.157	9.96×10^{9}	1.58×10^{-11}	2.04×10^{-04}
BFB	9.27	1.20×10^{8}	7.73×10^{-8}	1

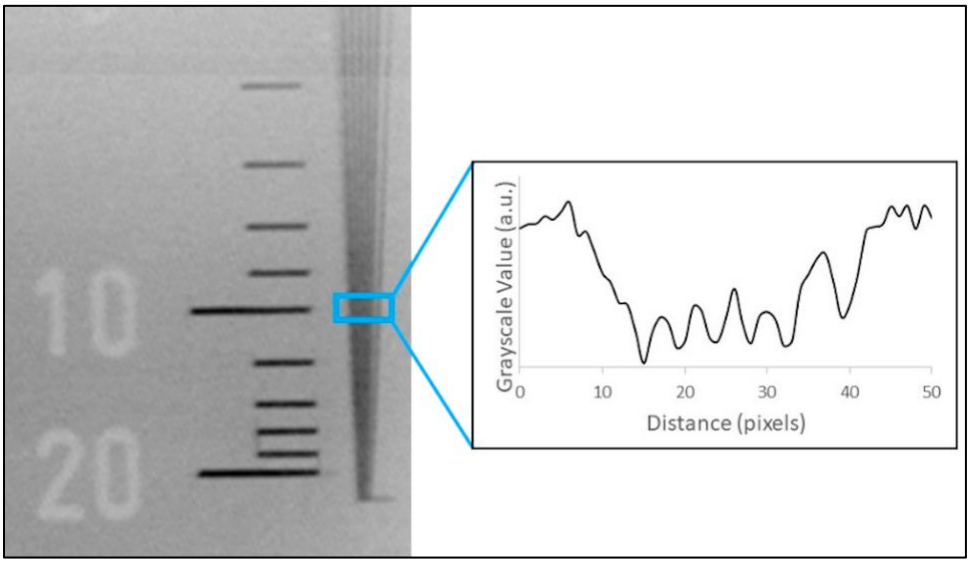

Figure 15. Radiograph of line-pair phantom recorded using an experimental storage phosphor plate and the corresponding profile taken at 10 lp/mm.

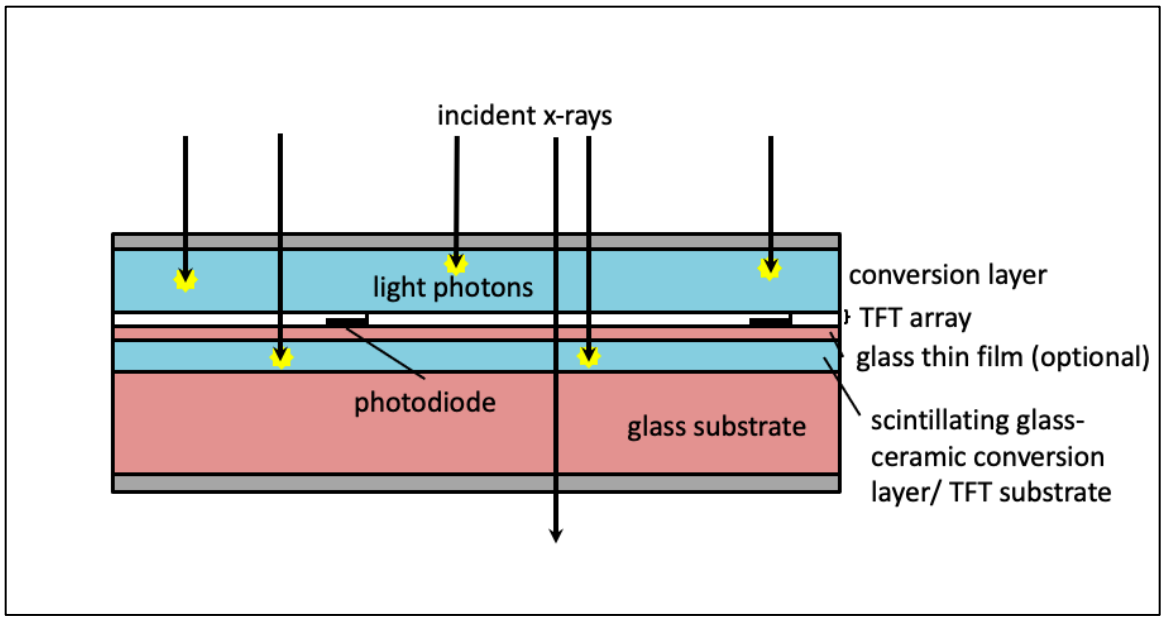

Figure 16. Cross-section view of dual-screen sandwich indirect flat panel detector displaying a scintillating conversion thin film coated on a glass substrate.

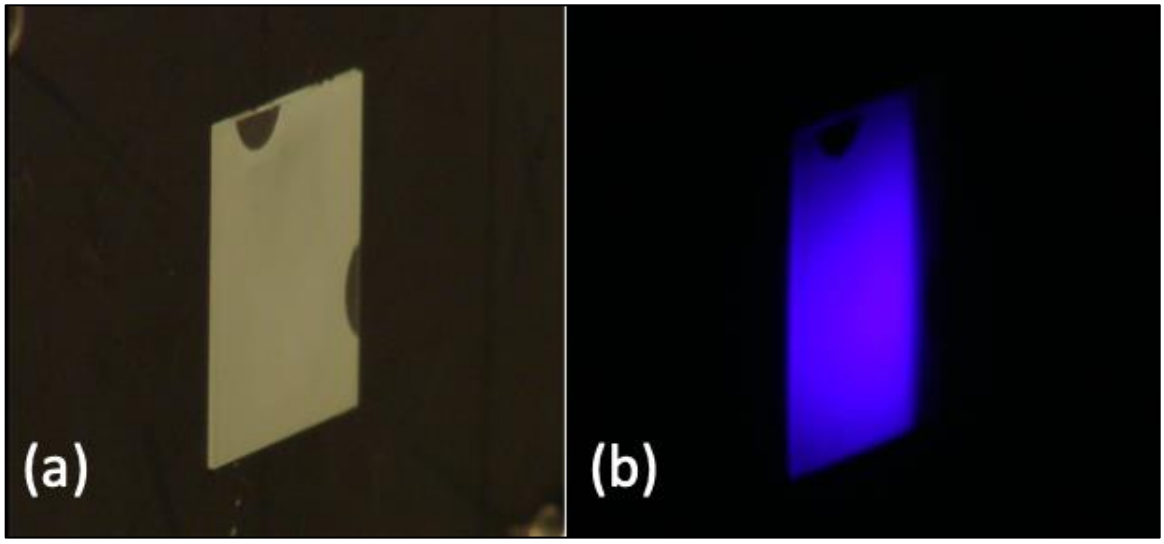

Figure 17. Scintillating thin film prototype in (a) visible light and (b) exposed to 45 keV x-rays.

CHAPTER II

OPTICAL PROPERTIES OF DIFFERING NANOLAYERED STRUCTURES OF EUROPIUM DOPED BARIUM FLUORIDE THIN FILMS SYNTHESIZED BY PULSED LASER DEPOSITION

C.W. Bond was responsible for the writing of this chapter and all research activities presented, except as noted: Y. Jin provided the TEM images. P. Gómez-Rodríguez assisted with PLD synthesis and emission measurements. J. Gonzalo, R. Serna, A.K. Petford-Long, R.L. Leonard, and J.A. provided guidance for the overall project and critical feedback.

Abstract

Optically-active thin films are employed in a variety of applications, such as LEDs and photovoltaics, due to their ability to act as up- or down-photon energy converters. Their performance depends critically on their composition and structure; thus, the use of novel synthesis techniques that allow for their control at the nanoscale level can result in improved efficiency and practicality. Layered thin films consisting of Eu-doped BaF_2 nanocrystalline layers separated by amorphous Al_2O_3 were synthesized via sequential pulsed laser deposition using three separate targets for the different components; this synthesis technique provides precise control of layer thickness at the nanoscale along with dopant distribution within the film. Cross-section transmission electron microscopy analysis verified the desired nano-layering. Post-deposition heat treatments in a nitrogen atmosphere resulted in samples exhibiting steady and robust emission with a broad peak ranging from 400-600 nm and a shoulder at 410 nm. The CIE 1931 chromaticity coordinates are x = 0.26-0.29 and y = 0.32-0.35 as a function of the sample configuration. Because the chromaticity coordinates are close to those of a pure white light (x = 0.33, y = 0.33), these films demonstrate properties advantageous for applications with UV-pumped white light LEDs.

Introduction

Light-emitting diode (LED) solid-state lighting boasts many advantageous characteristics including low energy consumption, high brightness, and a long lifetime [60-62]. Currently, the most common commercially-available white-LEDs use an InGaN chip, which produces blue light, combined with the phosphor YAG: Ce^{3+}, which downshifts a portion of the blue emission to create broadband emission [63-65]. A white light LED producing broadband

visible emission and incorporating a single-phase host material would result in a simpler manufacturing process. Different materials are being investigated to improve commercially-available white-LEDs [56]. A possible concept that is in its infancy of development is an ultraviolet (UV)-pumped white-LED, in which UV photons are downshifted to provide broadband visible emission [66].

Although the recent progress of LED research has mainly been focused on general lighting applications, there are many different health care applications that can benefit from the advantageous characteristics of LEDs compared to other light sources. As detailed in Dong and Xiong [17], LEDs have potential applications in medical imaging, light therapies, and photo-biomodulations. White LEDs have been combined with blue-light lasers to bypass the use of filters and mechanically-rotating wheels to give optimal signal-to-noise ratio in multi-spectral imaging [67, 68]. LED therapies with emissions in the visible range have proved to be beneficial in treating a broad range of medical conditions including Parkinson's disease, osteoporosis and inflammation, and in wound healing [21, 69, 70].

Divalent europium can present broadband emission that is highly susceptible to crystal field splitting [71]. The broad tunable emission has made Eu^{2+} a popular doping candidate for single-phase host materials with white-LED applications [72]. The Eu^{2+} emission is associated with the $4f^6 5d^1$ to $4f^7$ electron transition which occurs in the outer orbitals [54]. The location of this transition allows coordinate surroundings of the host to influence the energy of the emitted photon [56]. Changes in the nephelauxetic effect of different host lattices along with crystal field splitting allow Eu^{2+} emission to emit over the range of ultraviolet to red light [73]. The effects of crystal field splitting on Eu^{2+} emission is illustrated in Figure 18.

Glass-ceramics containing rare-earth doped fluoride crystalline material have been developed for potential applications such as wavelength shifters for solar cells and LEDs [46, 74]. The low phonon energy fluoride nanocrystalline matrix provides a favorable host for rare-earth dopants [75, 76]. Likewise, an oxyfluoride amorphous material provides a

low phonon energy environment advantageous for optically-active dopants [77]. It has been shown that when europium is added to aluminum oxide, the Al^{3+} cation facilitates the reduction of Eu^{3+} to Eu^{2+} to develop materials capable of broadband emission ideal for white light LED applications [78, 79]. Their performance depends critically on their composition and structure; thus, the use of novel synthesis techniques that allow for control at the nanoscale level can result in improved efficiency and practicality.

In this study, optical behavior of thin films with layers of nanocrystalline BaF_2, amorphous Al_2O_3, and a europium dopant, were synthesized by using sequential pulsed laser deposition. This synthesis technique provides precise control of layer thickness at the nanoscale level along with dopant distribution within the film. The amorphous Al_2O_3 layers contribute to encapsulating the fluoride host to prevent oxidation, which can limit optical performance. Different nanolayered structures were synthesized and photoluminescent (PL) emission measurements were obtained using a 355 nm excitation laser to determine the ability of the material to act as a UV-pumped LED. While all three experimental sample structures show promising optical characteristics for UV-pumped, white-LED applications, the differences in the nanolayered structures give a better understanding as to how the emission is affected by the Eu^{2+} coordinate environment. Cross-section transmission electron microscopy (TEM) analysis was conducted to verify the nanolayered structure of the samples. A complementary article focusing on BaF_2 the structural evolution and film growth of BaF_2 films deposited by controlled PLD conditions will be published.

Materials and Methods

Commercially available targets of Al_2O_3**,** BaF_2, and Eu_2O_3 were ablated to produce layered thin films via pulsed laser deposition (PLD). The pressure in the system was maintained at below 3.0×10^{-6} Torr during deposition. An ArF excimer laser with a 193 nm wavelength beam with a rated pulse length of 20 ns was used. Films were deposited on single side polished, 475-575 µm thick, test grade silicon wafers in the <100> crystalline orientation. The substrates were cleaned with an acetone rinse, ultrasonically in ethanol for 5 minutes, then dried with compressed nitrogen prior to their placement in the deposition chamber.

Al_2O_3, BaF_2, and Eu_2O_3 deposition parameters are detailed in Table 2. The different substrates positions are illustrated in Figure 19.

Three different layer configurations were designed in order to explore the Eu doping of BaF_2 (Structures 1 and 3) and the potential of having the Eu doping at the BaF_2/Al_2O_3 interface (Structure 2). Schemes of the structure of the different sample are shown in Figure 20.

Sample Structure 1 (Figure 20(a)) was synthesized by sandwiching an Eu_2O_3 layer between two BaF_2 layers and the Al_2O_3 matrix layers. An initial 2000 laser pulses were used on the Al_2O_3 target, followed by 2140 laser pulses on BaF_2, 430 laser pulses on Eu_2O_3, and 2140 laser pulses on BaF_2. This sequence ($Al_2O_3/BaF_2/Eu_2O_3/BaF_2$) was initially repeated 5 times and a final 2000 pulse Al_2O_3 layer was grown as a protective cap. At this point in the process, a sample was removed from the deposition chamber, and an additional 5 layers with a final cap was grown on top of a sample that remained in the chamber.

Sample Structure 2 (Figure 20(b)) was synthesized by depositing an Eu_2O_3 layer on top of BaF_2 layers with Al_2O_3 base layers. An initial 2000 laser pulses were used on the Al_2O_3 target, followed by 4280 laser pulses on BaF_2 and 430 laser pulses on Eu_2O_3. This sequence ($Al_2O_3/BaF_2/Eu_2O_3$) was initially repeated 5 times and a final 2000 pulse Al_2O_3 layer was grown as a protective cap. Identical to the previous structure, a sample with 5 layers and another sample with 10 layers were grown.

Sample Structure 3 (Figure 20(c)) was synthesized by alternating BaF_2 and Eu_2O_3 between Al_2O_3 layers. After an initial 2000 laser pulses on the Al_2O_3 target, 1710 laser pulses were used on the BaF_2 target, followed by 100 laser pulses on the Eu_2O_3 target. The BaF_2/Eu_2O_3 sequence was repeated 10 times and a final 2000 pulse Al_2O_3 layer was grown as a protective cap. A sample was kept with 1 ($Al_2O_3/(BaF_2/Eu_2O_3)$ x10) sequence and 2

additional sequences were grown on a separate sample, resulting in a total of 3 repeating sequences.

Cross-section TEM samples were prepared from Sample Structure 1 films by focused ion beam (FIB) milling. To protect the films from FIB damage, the samples were coated with a layer of Au using electron-beam evaporation before milling. TEM was carried out using a JEM-2100F instrument with 200 kV incident electron energy, in order to investigate the structure of the cross-section samples.

Heat treatments were performed in both ambient atmosphere and using nitrogen purge gas to determine the effects of the different heat treatment conditions. Samples that were heat treated in an ambient atmosphere will be referred to as (amb) and samples heat treated in a nitrogen atmosphere will be referred to as (N_2). The ambient atmosphere heat treatments were performed in a MESTRA HP-25 muffle furnace. The heat treatments in a nitrogen atmosphere were performed in a Thermconcept 50/250/12 tube furnace using a lab-grade N_2 purge gas. In both atmospheres, the samples were heat treated at a heating ramp of 10 K/ min to 300 °C, and held at that temperature for 1 hour, then allowed to cool to ambient temperature over time.

After the emission from the different sample structures were compared, the best sample configuration for UV-pumped white light LEDs was determined. Using this configuration, the emissions of a sample with 5 repeating sequences and 10 repeating sequences were compared to determine the effect of layer numbers on emission intensity. In addition, both samples were heat treated to 300 °C in a nitrogen atmosphere for 1 hour. Following the post-deposition heat treatments, emission data were collected, and emission intensities were compared.

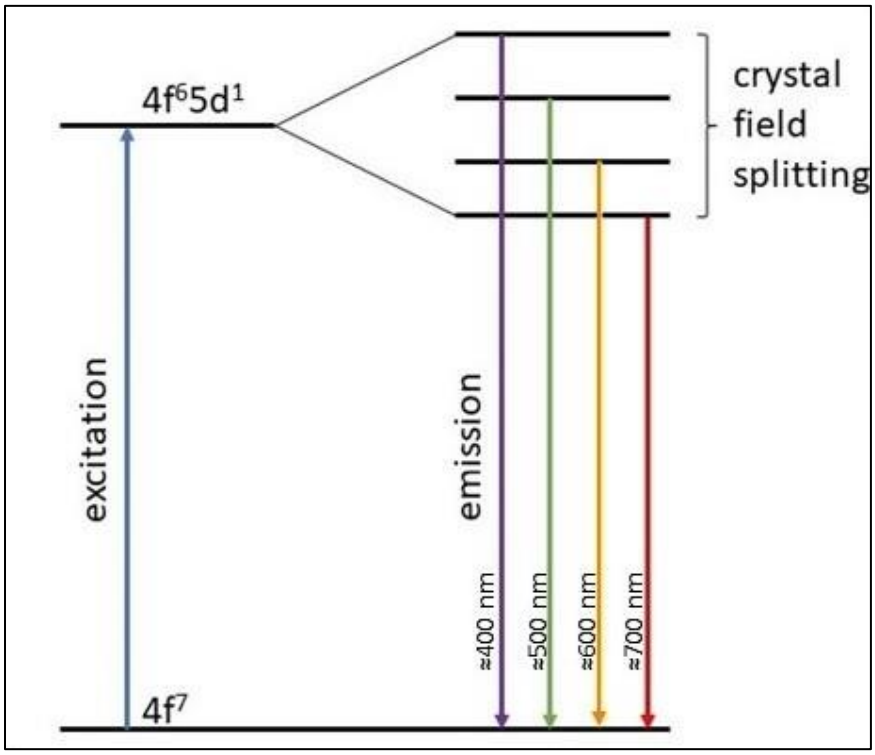

Figure 18. Partial energy level diagram of Eu^{2+} demonstrating how broadband emission is an outcome of crystal field splitting.

Table 2. PLD parameters of all of the materials that were ablated.

Material	*Laser Fluence*	*Laser Frequency*	*Substrate Position*[a]	*Target-substrate Distance*
Al_2O_3	4.7 J·cm^{-2}	20 Hz	20 °	37.8 mm
BaF_2	4.7 J·cm^{-2}	10 Hz	180 °	86.0 mm
Eu_2O_3	1.3 J·cm^{-2}	10 Hz	20 °	37.8 mm

[a] Substrate position is angle off-axis relative to the shared axis position.

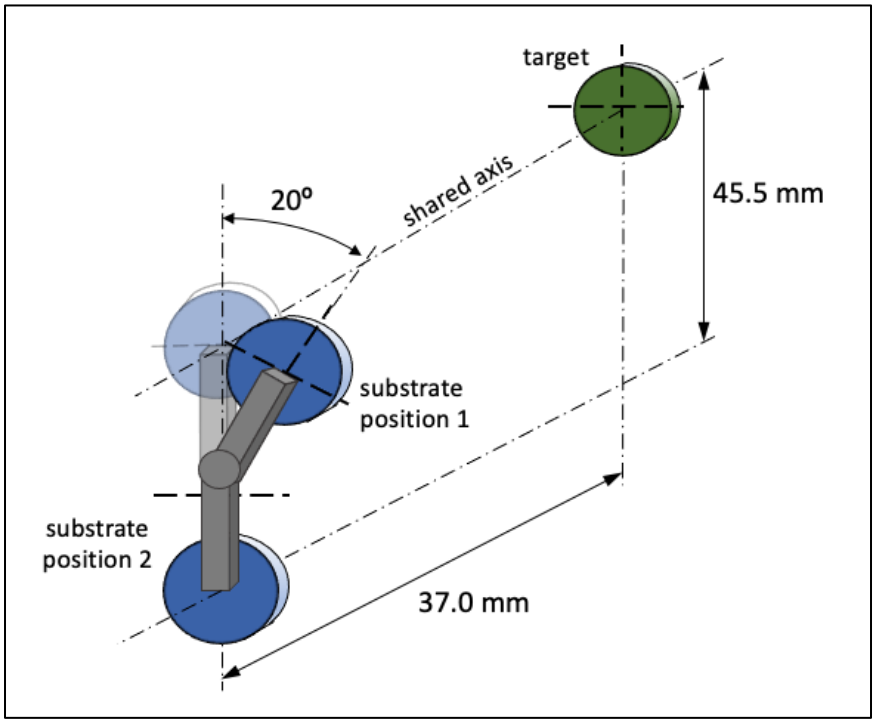

Figure 19. Illustration displaying different substrate positions used to deposit Al_2O_3 and Eu_2O_3, rotated 20° from the conventional 90° perpendicular to the target (substrate position 1), and BaF_2, rotated 180° from the conventional 90° perpendicular to the target (substrate position 2).

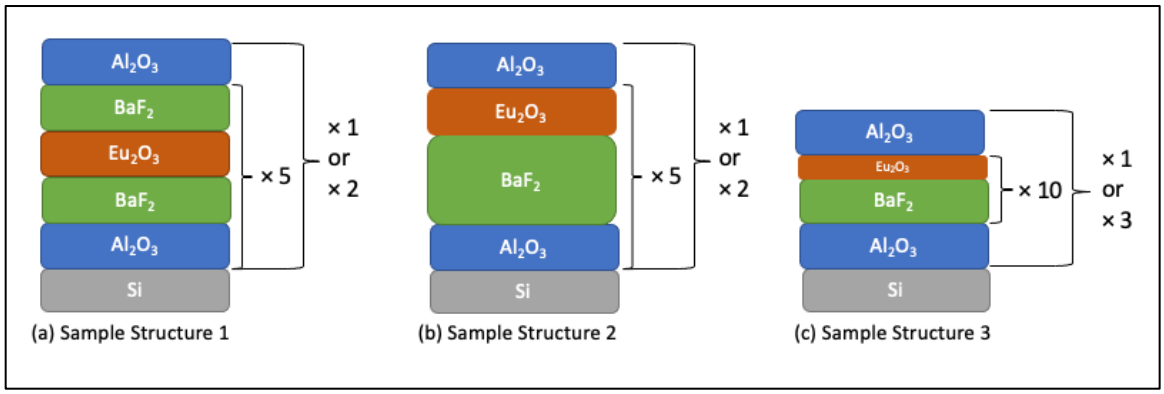

Figure 20. Illustration of different thin film layer configurations synthesized to investigate dopant incorporation. (a) Sample Structure 1, (b) Sample Structure 2, and (c) Sample Structure 3.

Photoluminescence studies were conducted by using a 355 nm Genesis CX 355-200 Optically Pumped Semiconductor Laser (Coherent) with a power of approximately 8 mW as the excitation source. A monochromator (ActonSpectraPro300i, diffraction grating= 1200 g/mm (Vis)) filtered the light emitted by the samples, which was detected through a photomultiplier tube (EMI9659QB-S20). In addition, the signal was amplified with a standard lock-in technique. CIE 1931 chromatic coordinates were obtained by processing the emission data in Origin 2021 version 9.8 (OriginLab) and utilizing the Chromaticity Diagram v1.1 application.

Results and Discussions

Microscopy

Cross-section TEM analysis verified that the films were grown with the intended layered nanostructures. Figure 21 shows a TEM cross-section of Structure 1 as-made with 5 and 10 layers. Both samples show clear layering with the layers being uniform throughout the film. The darker contrast layers correspond to the Eu_2O_3 deposits, the lighter contrast layers are attributed to Al_2O_3, and the BaF_2 shows an intermediate contrast. The 5-layer film has a total thickness of 50 nm and the 10-layer sample has a total thickness of 99 nm. The 10-layer film (Figure 21(b)) presents an anomaly in the multilayer periodicity, two layers down from the gold protective cap, where the layer does not show the dark contrast associated with Eu_2O_3. This is hypothesized to be due to experimental error, possibly a malfunction of the stepper motor that controlled the target position, resulting in Eu_2O_3 not being ablated for that layer. The wide light layer in the middle of the sample seen in Figure 21(b) is because of the double thickness of Al_2O_3 deposited between the first and second 5 repeat sequences (see Figure 20(a)).

Optical characterization

The emission spectra of the three as-deposited sample structures are shown in Figure 22. The three sample structures resulted in distinctly different PL emissions. These differences demonstrate the consequence of their structural configuration on the emission of these

materials. Structures 1 and 2 were synthesized with the same amount of Al_2O_3, BaF_2, and Eu_2O_3, with the only difference coming from the fact that in Structure 1, the Eu_2O_3 is sandwiched between two BaF_2 layers in each repeat, yet a difference in emission is seen. The layer sequence determines the local coordination environment of the luminescent center (Eu), which can be manipulated depending on the desired emission.

The emission spectra for Sample Structure 1 with 5 layers as-made and heat treated are shown in Figure 23. The as-made sample did not exhibit any measurable emission expected from crystalline BaF_2, thus indicating that all of the layers in the sample were amorphous, which was verified by electron diffraction patterns and detailed in the complementary article. A peak at 410 nm and a broad emission from 450 – 600 nm is seen in Structure 1 (amb). The 410 nm peak can be attributed to the $4f^6 5d^1$ to $4f^7$ transition of Eu^{2+} incorporated in BaF_2 nanocrystals. The authors hypothesize that the broad emission from 400 – 600 nm can be attributed to Eu^{2+} in different environments such as the BaF_2 nanocrystalline matrix, the BaF_2/Al_2O_3 interface, and the Al_2O_3 layers as shown in Figure 24. In Structure 1 (N_2), the intensity of the broad emission increases, and the 410 nm emission is expressed as a shoulder indicating the movement of the Eu dopant into different environments.

The emission spectra for Sample Structure 2 with 5 layers as-made and heat treated are shown in Figure 25. The as-made film exhibited a broad emission centered at 540 nm. The spectrum of Structure 2 (amb) shows a 410 nm peak along with a broad emission that is comparable to Structure 1 (amb). Structure 2 (N_2) exhibits a broad emission from 400 – 600 nm and a shoulder at 410 nm is shown, but of lesser intensity when compared to Structure 2 (amb). Both the emission spectra of Structure 2 (N_2), and Structure 2 as-made, exhibit a slight peak at 610 nm that can be attributed to a $^5D_0$ to $^7F_2$ electron transition of Eu^{3+} [80]. This sample structure had the largest amount of Eu_2O_3/Al_2O_3 adjacent layers, which could prevent Eu from migrating into a reducing atmosphere due to the smaller percentage of adjacent BaF_2/Eu_2O_3 layers or the amount of oxygen present in the Al_2O_3 layers.

The emission spectra for Sample Structure 3 with 5 layers as-made and heat treated are shown in Figure 26. Unlike the previous two sample structures, the as-made Structure 3 exhibited the most intense emission when compared to the emissions after heat treatment. A sharp peak at 410 nm with a broader peak at 430 nm was found. Growing thicker layers of BaF_2 resulted in the layers being nanocrystalline as deposited, which then were able to luminesce prior to any post-synthesis heat treatment. With the Structure 3 (amb) emission, the 410 nm peak intensity decreased resulting in a broader, less intense, peak with a range from 400 - 500 nm. A broad emission with consistent intensity between 400 - 650 nm was measured in Structure 3 (N_2).

The 410 nm peak, attributed to BaF_2:Eu^{2+}, is seen in all three structures following heat treatment in an ambient atmosphere. This result shows that heat treatments facilitated Eu diffusion into the BaF_2 matrix and could have resulted in oxygen-aided emission quenching in the Al_2O_3 layers. Structure 3 exhibits the most intense BaF_2:Eu^{2+} emission due to an increased percentage of adjacent Eu_2O_3/BaF_2 layers when compared to Structure 1 and 2. The authors hypothesize that broadening of the emission peaks following heat treatments in an inert atmosphere could be caused by the Eu dopant diffusing into Al_2O_3 layers, but without the emission quenching that was found with ambient atmosphere heat treatments. The dramatic changes in the emission of Structure 3, a structure with a relatively small amount of Eu/Al_2O_3 adjacent layers, found after different heat treatment conditions, support this hypothesis.

When repeated emission measurements were conducted at the same sample location on films that had been heat treated in an ambient atmosphere, the emission intensity decreased as demonstrated by Structure 1 in Figure 27. The longer the excitation laser was focused on the same location, the more the emission intensity decreased. A decrease in emission intensity due to UV laser degradation was found for all sample structures following post synthesis heat treatments in an ambient environment and is repeatable for different sample locations. The main proposed mechanism in the literature for the degradation is photogeneration of defects [81, 82]. When Structure 1 was heat treated in nitrogen, no

emission degradation occurred after exposure to the UV excitation laser, as shown in Figure 28. This could be related to the passivation of the Eu with nitrogen bonds, which leads to samples with a very robust response. These results agree with the work conducted by Amidani et al. [83], who stated that oxidation of Eu^{2+} to Eu^{3+} is the main mechanism that results in emission quenching. Further studies need to be conducted to determine if the degradation of these samples is reversible through heat treating or laser stimulation.

Since emission intensity that does not significantly diminish overtime is necessary for the proposed LED application, and we have seen that the emission stability against UV laser degradation of the samples heat treated in nitrogen was superior to that of samples subject to an ambient atmosphere, we have only analyzed the chromatic coordinates of the nitrogen heat-treated samples. The chromatic coordinates of all three sample structures following a 1-hour, 300 °C post-synthesis heat treatment in nitrogen, using CIE 1931, are shown in Figure 29. The coordinates were (x = 0.26, y = 0.33) for Structure 1, (x = 0.26, y = 0.32) for Structure 2, and (x = 0.29, y = 0.35) for Structure 3. Pure white CIE 1931 chromatic coordinates are considered to be (x =0.33, y = 0.33). The chromatic coordinates show that all three sample structures emit white light that could be used for UV-pumped, white-LED applications. Structure 1 (N_2) exhibits a white light emission that was more intense and had the best emission stability against UV laser degradation when compared to that of Structures 2 and 3; therefore, Structure 1 is the best layer configuration for the intended application.

The emission spectra of Structure 1 (N_2) consisting of 5 layers and 10 layers are shown in Figure 30. The emission exhibited a 39% increase in intensity at 472 nm when the number of layers doubled from 5 to 10. This demonstrates an increase of light output from the films when more material is deposited. The increase in emission due to increase in the number of layers is expected to reach an asymptote due to self-absorption. Although the emission intensity was increased, the emission spectrum became less favorable for white light applications. The spectrum exhibited a broad emission throughout the entire measured range, showing a broad apex peak from 440 – 460 nm, a shoulder at 410 nm, and a broad

shoulder near 500 nm. This emission demonstrates chromaticity coordinates of (x = 0.25, y = 0.32).

Conclusion

Nanolayered barium fluoride/ europium oxide/ aluminum oxide films were synthesized via sequential pulsed laser deposition using three different layer configurations. Cross-section TEM analysis of the samples showed that the layers are uniform throughout the film. The different sample structures were subjected to post-synthesis heat treatments in ambient and nitrogen atmospheres to precipitate optically-active nanocrystals. Photoluminescent emission was measured from the samples, both as-made and following heat treatments. All sample structures subject to ambient atmosphere heat treatments exhibited emission degradation when subject to the excitation laser. However, it is found that with heat treatments in a nitrogen atmosphere this degradation can be suppressed. Sample Structure 1, consisting of europium sandwiched between barium fluoride layers, was determined to be the best performing structural configuration based on its emission intensity and stability against UV laser degradation; after heat treatment in nitrogen, the film exhibited a broad emission from 400 - 600 nm with a shoulder at 410 nm. Chromaticity coordinates plotted from the acquired emission spectra ranged from x = 0.26-0.29 and y = 0.32-35, which demonstrates a potential application in UV-pumped white light LEDs. Emission intensity was compared to film thickness to show a 39% increase in light output when the number of sample layers was doubled from 5 to 10.

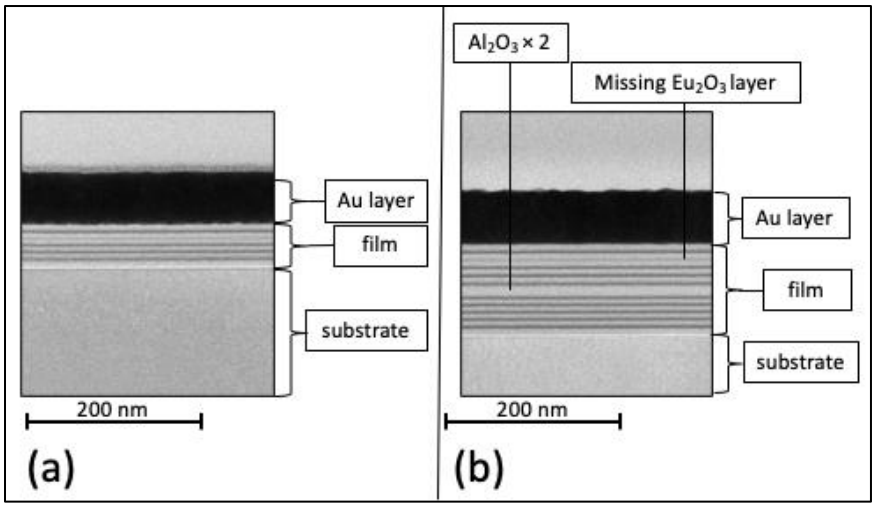

Figure 21. TEM cross-section images of as-made Sample Structure 1 $Al_2O_3/BaF_2/Eu_2O_3$ thin films synthesized with (a) 5 layers and (b) 10 layers.

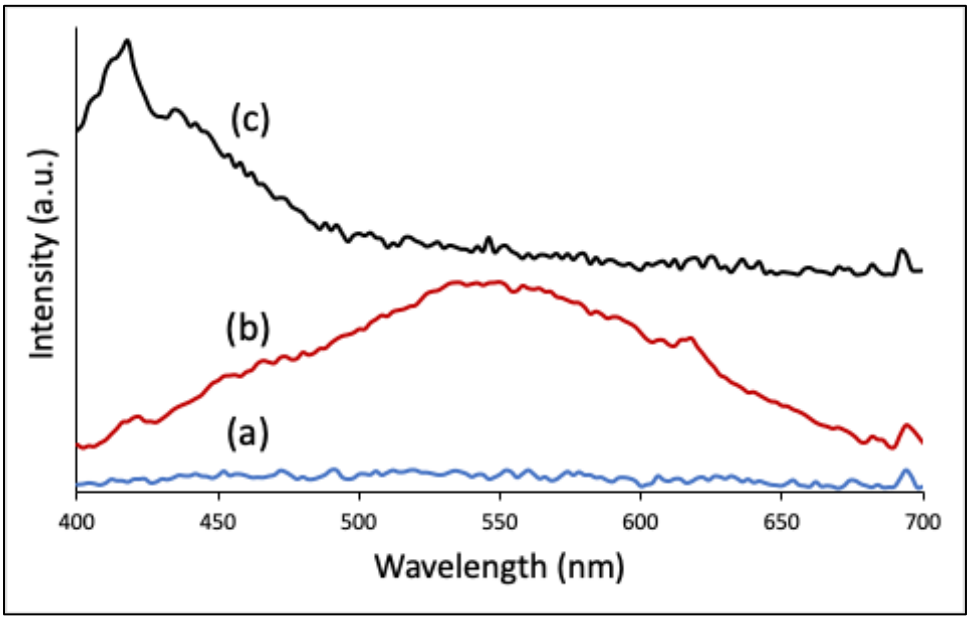

Figure 22. Emission spectra from a 355 nm excitation source for as-made (a) Structure 1 with 5 layers, (b) Structure 2 with 5 layers, and (c) Structure 3 with 1 layer.

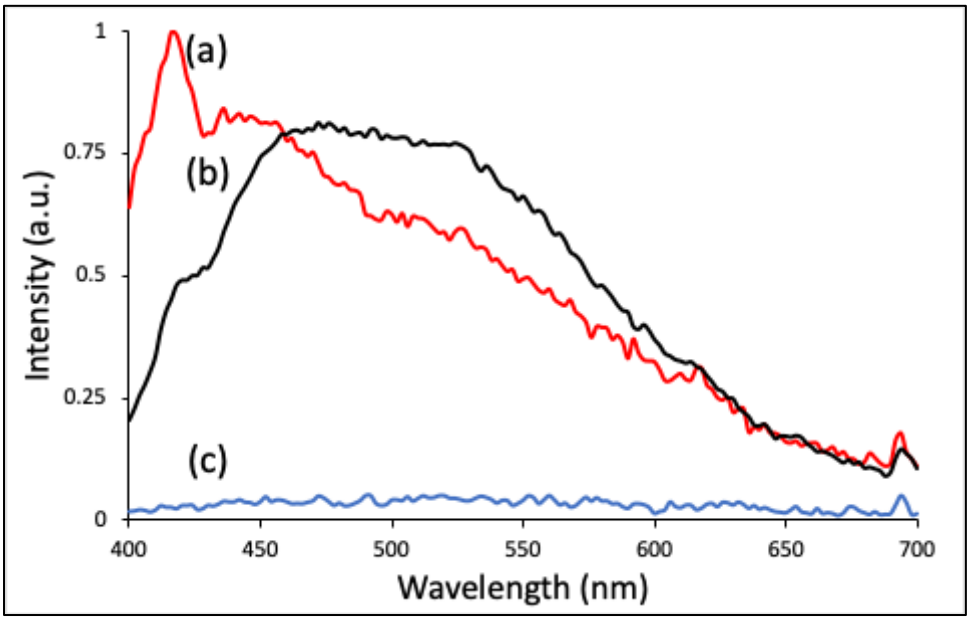

Figure 23. Emission spectra of Sample Structure 1 with 5 layers from 355 nm excitation source after (a) 1-hour heat treatment at 300 °C in ambient atmosphere, (b) 1-hour heat treatment at 300 °C in a nitrogen atmosphere, and (c) as-made sample.

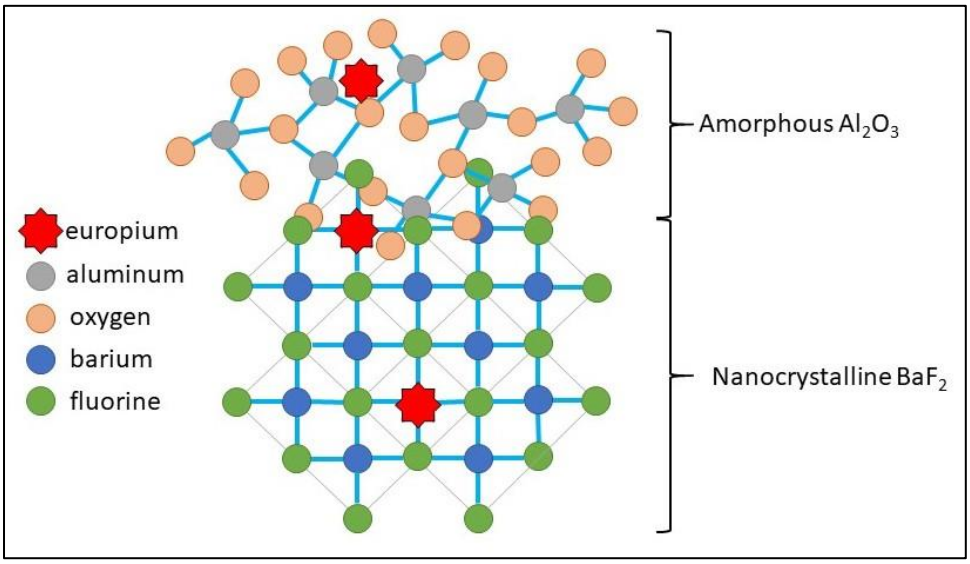

Figure 24. Illustration showing atomic layers of a barium fluoride/aluminum oxide thin film and three different possible locations of a europium dopant.

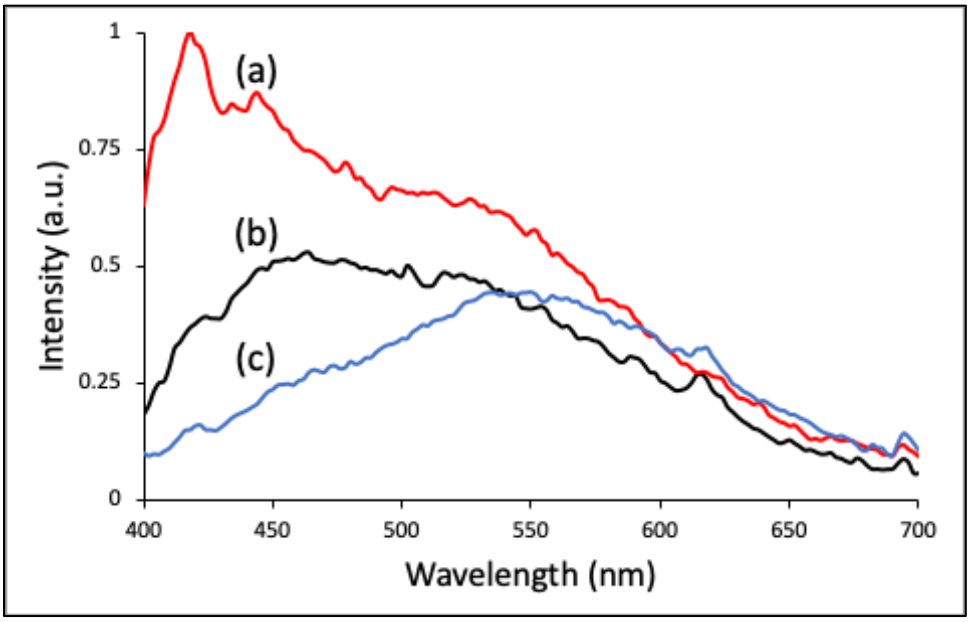

Figure 25. Emission spectra from a 355 nm excitation source for Sample Structure 2 with 5 layers after (a) 1-hour heat treatment at 300 °C in ambient atmosphere, (b) 1-hour heat treatment at 300 °C in a nitrogen atmosphere, and (c) as-made.

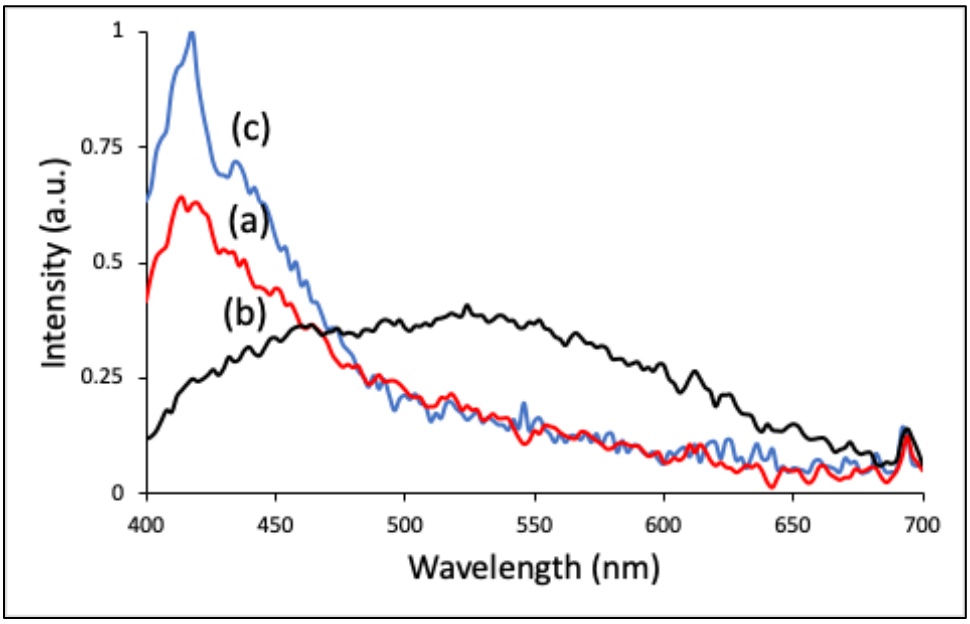

Figure 26. Emission spectra of Sample Structure 3 with 5 layers from 355 nm excitation source after (a) 1-hour heat treatment at 300 °C in ambient atmosphere, (b) 1-hour heat treatment at 300 °C in a nitrogen atmosphere, and (c) as-made sample.

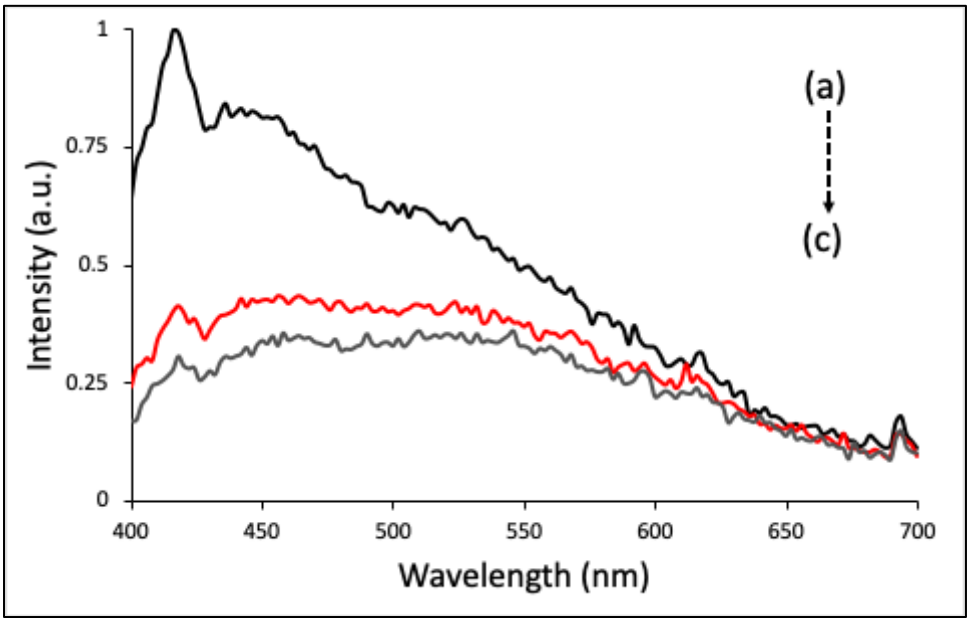

Figure 27. Emission spectra of Sample Structure 1 with 5 layers from a 355 nm excitation source after a 1-hour, 300 °C post-synthesis heat treatment in an ambient atmosphere. The spectra were obtained from consecutive measurements at the same sample location. Spectrum (a) is the first measurement, (b) is the second measurement, and (c) is the third measurement.

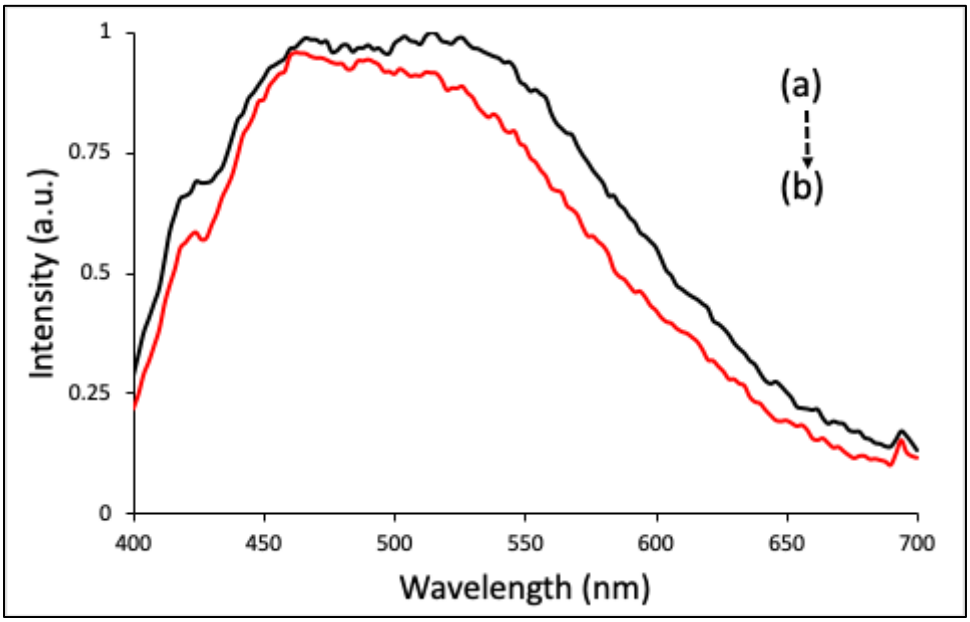

Figure 28. Emission spectra of Sample Structure 1 with 5 layers from a 355 nm excitation source after a 1-hour, 300 °C post-synthesis heat treatment in a nitrogen atmosphere. The spectra were obtained from consecutive measurements at the same sample location. Spectrum (a) is the first measurement and (b) is the second measurement.

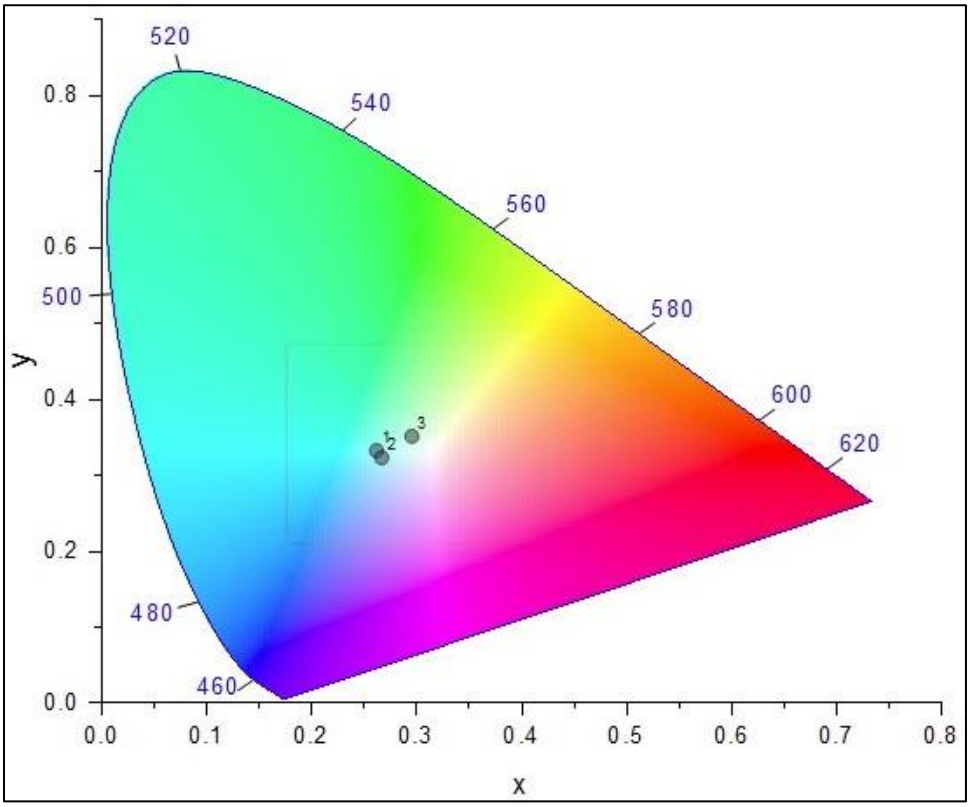

Figure 29. Color points in the CIE 1931 chromaticity diagram of (1) Sample Structure 1, (2) Sample Structure 2, and (3) Sample Structure 3 after a 1-hour heat treatment at 300 °C in a nitrogen atmosphere.

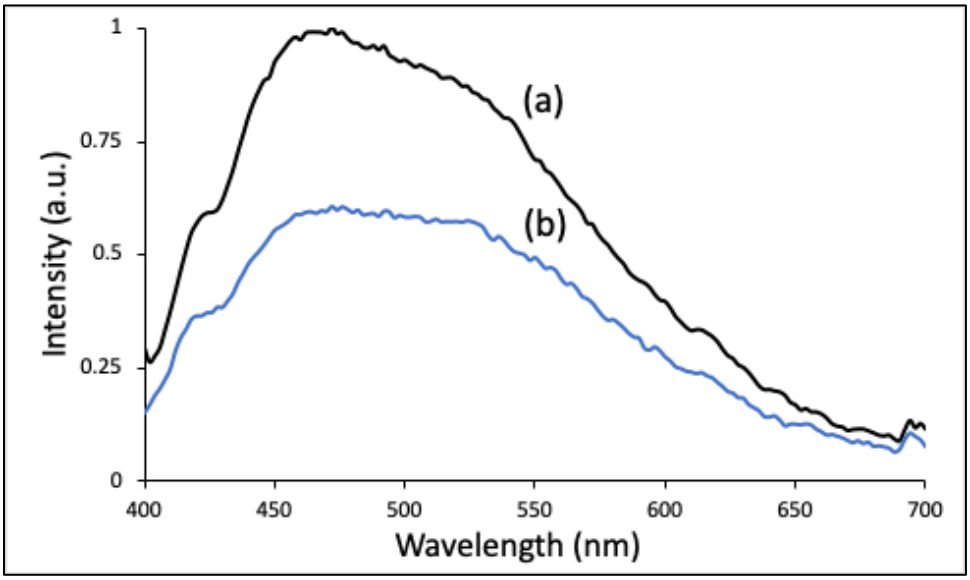

Figure 30. Emission spectra of Sample Structure 1 from a 355 nm excitation source with a sample containing (a) 10 layers and (b) 5 layers.

CHAPTER III

OPTICAL CHARACTERIZATION OF ALUMINUM OXIDE/ BARIUM FLUORIDE LAYERED THIN FILMS CODOPED WITH EUROPIUM AND MANGANESE SYNTHESIZED BY PULSED LASER DEPOSITION

C.W. Bond was responsible for the writing of this chapter and all research activities presented, except as noted: P. Gómez-Rodríguez conducted PLD synthesis and emission measurements. J. Gonzalo, R. Serna, A.K. Petford-Long, R.L. Leonard, and J.A. Johnson provided guidance for the overall project and critical feedback.

Abstract

The Eu^{2+}/Mn^{2+} complex is a popular dopant option in white light applications due to the broadband emission of the Eu^{2+} ion and the red component of the Mn^{2+} ion. Codoping europium with manganese has the potential to increase emission intensity and provide a purer white light when compared to singly doped Eu material. This study investigates the optical effect of manganese on europium doped BaF_2/Al_2O_3 layered thin film synthesized by pulsed laser deposition. Using a layered configuration determined in previous studies, two different amounts of manganese were introduced into the films using an MnO target. The samples were subject to post-deposition thermal treatments in a nitrogen atmosphere, then emission measurements were conducted using a 355 nm excitation laser. The sample with a 1:8 Mn/Eu ratio showed no change in emission trends when compared to a sample with only Eu dopant. The sample with a 1:2 Mn/Eu ratio showed a blue shift in emission with chromic coordinates of x= 0.23 and y= 0.26, which could be advantageous for applications with UV-pumped blue-light LEDs.

Introduction

The use of transition metals is favorable for solar cell, semiconductor, and optical devices due to their large tunable bandgap and physical properties arising from the localized character of d-elections [84, 85]. The transition of an electron from an excited state to a ground state, or in terminology used for band gaps, from a conduction band to a valence band, can produce the emission of a photon i.e. luminescence. The optical performance of

the Mn^{2+} ion relies on 3d-3d electron transitions which are forbidden by the Laporte selection rule which states a change in parity must occur for allowed transitions. The Mn^{2+} ion is nearly colorless with poor emission performance which restricts its applications in luminescent materials [8, 86, 87]. The Laporte rule can be relaxed by coupling of the electronic transition with vibrations to result in a loss of symmetry, but the Mn^{2+} ion is typically paired with a sensitizer to increase optical performance [88].

The Eu^{2+} ion is a popular sensitizer to an Mn^{2+} activator that has yielded desirable photoluminescent properties in several host lattices [89-91]. Even at low dopant concentrations, the Eu^{2+} to Mn^{2+} energy transfer has been observed in many different halide crystal matrices [92-95]. An excited $5d^1$ electron in Eu^{2+} can be at the $^6P_{5/2}$ or $^6P_{7/2}$ energy level, which is similar to the $^4E(^4D)$ energy level in an excited Mn^{2+} ion [96]. The similar energy levels allow for an electron transfer from Eu^{2+} to Mn^{2+} and emission from the Mn^{2+} ion through a mechanism illustrated in Figure 31. Emission from Mn^{2+} is typically in the red region of the visible spectrum but can range from 500 – 700 nm depending on the crystalline matrix it occupies. The Eu^{2+}/Mn^{2+} dopant complex is a popular phosphor material for LED applications: Eu^{2+} contributes to broad emission in the blue region of the visible spectrum while Mn^{2+} contributes to broad emission in the red region resulting in a high-quality white-light LED.

The optical influence of the transition metal manganese is presented in this study by characterizing two samples with different amounts of MnO added to nanolayered thin films. The layered configuration and post-synthesis heat treatments used were based on results from Chapter II. One sample was synthesized with a 1:8 Mn to Eu dopant ratio and one with a 1:2 Mn to Eu ratio. The ratios are based on the quantities of cations and assuming similar densities. Samples, as-made and following post-synthesis heat treatments, are compared by photoluminescent emission characterization achieved using a 355 nm excitation laser. The optical influence of the Mn dopant is determined by comparing the emission of a sample with only an Eu dopant. Comparing the two different amounts of

MnO in the samples demonstrates a threshold of material needed for Mn optical influence in the regions measured.

Materials and Methods

Commercially available targets of Al_2O_3**,** BaF_2, Eu_2O_3, and MnO were ablated to produce layered thin films via pulsed laser deposition (PLD). The pressure in the system was maintained below 3 x 10^{-6} Torr during deposition. An ArF excimer laser with a 193 nm wavelength beam with a rated pulse length of 20 ns was used. Films were deposited on single side polished, 475-575 µm thick, test grade silicon wafers in the <100> crystalline orientation. The substrates were cleaned with an acetone rinse, ultrasonically in ethanol for 5 minutes, then dried with compressed nitrogen prior to their placement in the deposition chamber.

Associated PLD set up for materials Al_2O_3, BaF_2, and Eu_2O_3 are detailed in Chapter II. The deposition parameters of the ablated materials, including MnO, are shown in Table 3.

Samples using the same layered configuration and two different Mn dopant amounts were grown, as illustrated in Figure 32.

Codoped Sample 1 (Figure 32(a)) was synthesized with a small amount of MnO relative to the amount of Eu_2O_3. An initial 2000 laser pulses were used on the Al_2O_3 target, followed by 4280 laser pulses on BaF_2, 430 laser pulses on Eu_2O_3, 100 laser pulses on MnO, and 4280 laser pulses on BaF_2. This sequence (Al_2O_3/BaF_2/Eu_2O_3/MnO/BaF_2) was repeated 5 times and a final 2000 pulse Al_2O_3 layer was grown as a protective cap. Based on preliminary *in situ* spectroscopic ellipsometry, the number of stated pulses will equate to layers of 10 nm Al_2O_3, 5 nm BaF_2, and 0.5 nm MnO.

Codoped Sample 2 (Figure 32(b)) was synthesized with a projected 1:1 Eu_2O_3 to MnO thickness ratio. An initial 2000 laser pulses were used on the Al_2O_3 target, followed by 4280 laser pulses on BaF_2, 430 laser pulses on Eu_2O_3, 400 laser pulses on MnO, and 4280

laser pulses on BaF_2. This sequence ($Al_2O_3/BaF_2/Eu_2O_3/MnO/BaF_2$) was repeated 5 times and a final 2000 pulse Al_2O_3 layer was grown as a protective cap. The project thickness of the layers is the same as Codoped Sample 1, except for a 2.0 nm layer of MnO instead of 0.5 nm.

The samples were heat treated in a nitrogen atmosphere at a heating ramp of 10 K/ min from ambient temperature to 300 °C and held at that temperature for 1 hour, then allowed to cool to ambient temperature over time.

Photoluminescence studies were conducted by methods detailed in Chapter II.

Results and Discussions

The emission spectra of Codoped Sample 1 synthesized with 0.5 nm of MnO as-made and following a 1 hour 300 °C heat treatment in a nitrogen atmosphere achieved by a 355 nm excitation wavelength is shown in Figure 33. The as-made sample exhibited a sharp peak at 418 nm and a steady decrease in intensity throughout the rest of the visible spectrum with the exception of a shoulder at 446 nm. The sample heat treated in a nitrogen environment exhibited a broad emission with the most intensity found between 450 and 550 nm. A shoulder is seen at 420 nm and a steady decrease in intensity is exhibited from 550 nm through the remainder of the visible spectrum.

The emission spectra of Codoped Sample 2 synthesized with 2 nm of MnO as-made, and following a 1 hour 300 °C heat treatment in a nitrogen atmosphere achieved by a 355 nm excitation wavelength are shown in Figure 34. When observing the 420-500 nm region, the sample heat treated in nitrogen exhibited an emission approximately four times greater than the as-made sample. The emission of both samples exhibited similar trends and spectral shapes. The most intense emission is exhibited in the 418-468 nm range with two broad peaks at 422 and 448 nm and a shoulder at 460 nm.

Table 3. PLD parameters of all of the materials that were ablated.

Material	*Laser Fluence*	*Laser Frequency*	*Relative Substrate Position*	*Target-substrate Distance*
Al_2O_3	8.0 J/cm^2	20 Hz	20 °	37.8 mm
BaF_2	8.0 J/cm^2	10 Hz	180 °	86.0 mm
Eu_2O_3	2.0 J/cm^2	10 Hz	20 °	37.8 mm
MnO	8.0 J/cm^2	10 Hz	20 °	37.8 mm

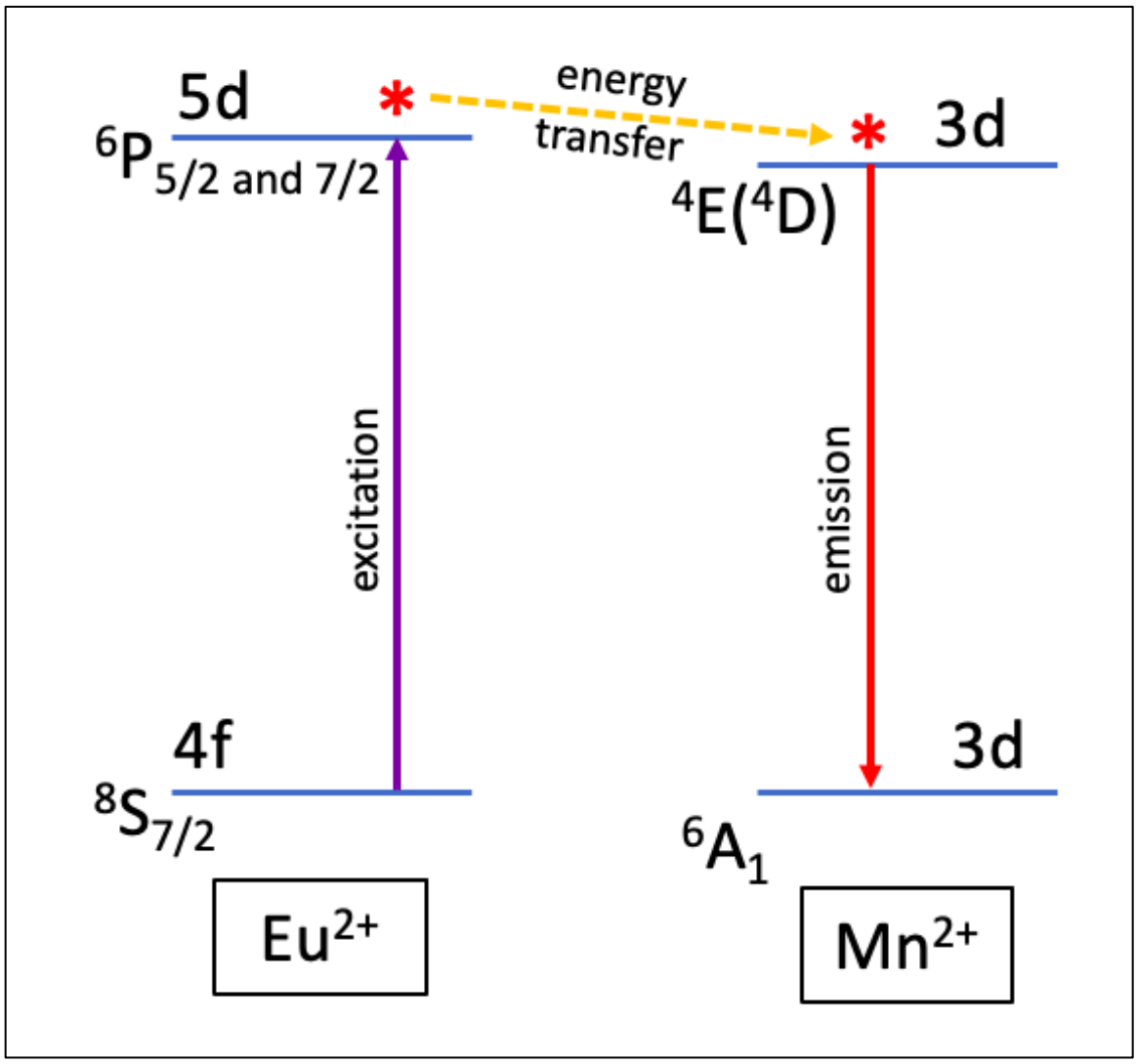

Figure 31. Illustration of a proposed mechanism of energy transfer between Eu^{2+} and Mn^{2+} ions.

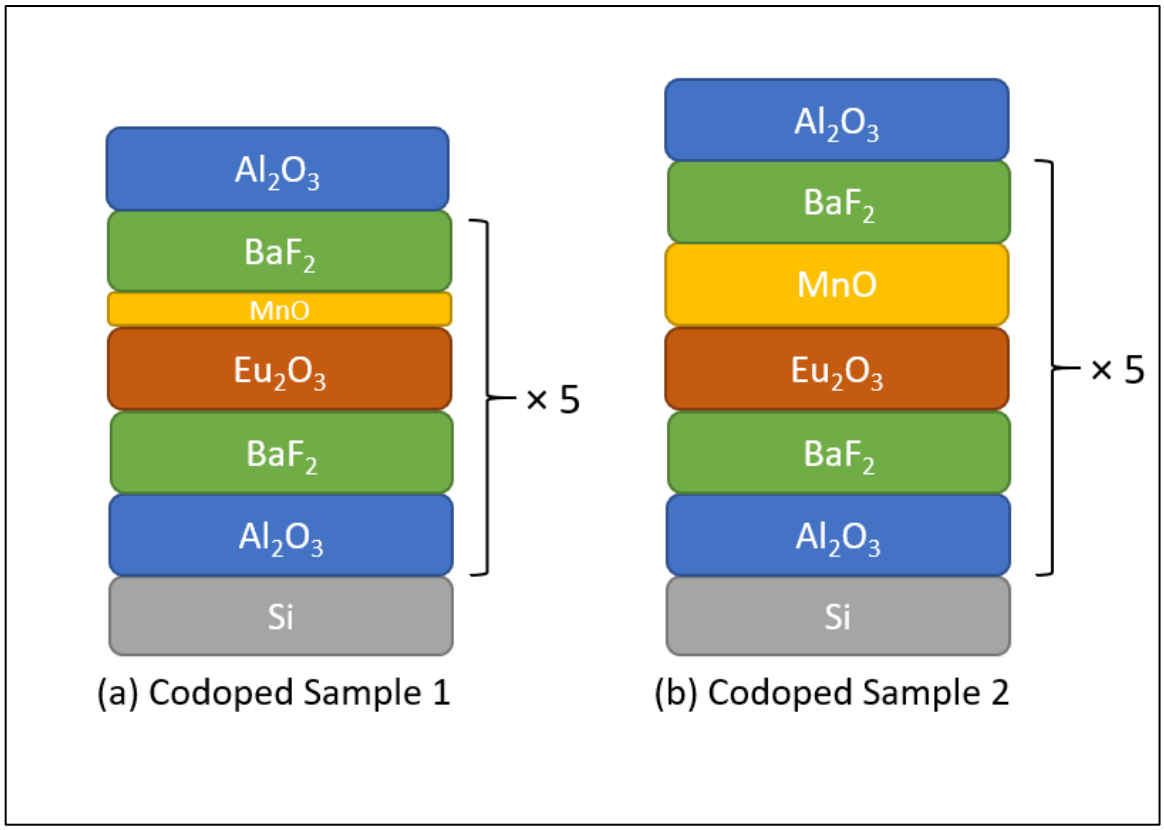

Figure 32. Illustration of samples with the same layered configuration and two different manganese dopant amounts.

The optical influence of the Mn dopant on the Eu/Mn complex is shown in Figure 35 by comparing the emission of the two codoped samples to a sample with only Eu (Sample Structure 1) from Chapter II. In the sample with 2.0 nm MnO, the first broad peak at 420 nm can be attributed to the $4f^6 5d^1$ to $4f^7$ electron transition of an Eu^{2+} ion in a BaF_2 matrix. This peak is similar to the emission of Eu-doped samples heat treated in an ambient atmosphere and aligns with the shoulders found in the emission of samples heat treated in a nitrogen atmosphere. The second broad peak can be attributed to either emission from Eu^{2+}/Mn^{2+} complexes or Mn_2O_3 nanoparticles [97, 98].

Because the phase diagram of Mn-O is comprised of MnO, MnO_2, Mn_2O_3, and Mn_3O_4, luminescence from Mn^{2+}, Mn^{3+}, and Mn^{4+} ions must be considered [99, 100]. Emission from the Eu^{2+}/Mn^{2+} complexes would indicate electrons transferring from the excited $^6P_{5/2}$ or $^6P_{7/2}$ energy state of Eu^{2+} to the excited $^4E(^4D)$ energy level of Mn^{2+} followed by the emission of photons. Emission from Mn_2O_3 nanoparticles could indicate oxygen vacancy-related defects. Emission from Mn^{4+} can be ruled out as it is usually exhibited in the near-infrared region [101, 102]. To confirm the origins of the emission, an excitation spectrum would need to be measured. A peak at approximately 300 nm is expected in the excitation spectrum in photoluminescence attributed to $^4E(^4D)$ energy levels [103]. Grazing incidence x-ray diffraction could be used to determine the presence of Mn_2O_3 nanoparticles.

The emission of the codoped sample with 0.5 nm MnO showed similar trends and intensities when compared to the sample only doped with Eu, indicating no optical influence of the Mn dopant. Because optical characteristics were changed with an increased amount of MnO, it is hypothesized the 0.5 nm sample did not contain enough Mn^{2+} or Mn^{3+} ions to yield a measurable emission. Using a PLD target that has more favorable stoichiometry to producing Mn^{2+} ions, such as MnF_2, could increase the optical influence of Mn with less ablated material. However, switching from an oxide to a fluoride target would introduce the disadvantage of increased material costs and the necessity for more intricate storage and handling procedures to avoid oxidation.

The chromatic coordinates of the two co-doped samples are plotted using CIE 1931 and shown in Figure 36. The emission of the 0.5 nm MnO sample had a similar trend to a sample with only Eu, so the chromic coordinates are identical (x=0.26, y=0.33) as expected. The coordinates of the sample with 2.0 nm MnO were (x= 0.23, y=0.26), which exhibits a blue-shift when compared to europium-doped samples. Because pure white CIE 1931 chromatic coordinates are (x=0.33, y=0.33), MnO dopant does not appear to be beneficial for UV-pumped white-LEDs, but which could be advantageous for applications with UV-pumped blue-light LEDs. Blue-light has shown to be beneficial for good health with increasing exposure improving alertness and subjective well-being [104].

Previous experiments demonstrated the possibility of decreased emission output with increased exposure time to an excitation source. The samples heat treated in a nitrogen atmosphere showed a steady emission intensity when exposed to an excitation laser source, which correspondences with results found in Chapter II. Figure 37 and Figure 38 show repeated emission measurements conducted on the same sample location for both co-doped samples.

Conclusion

A threshold range was found for the amount of manganese necessary to optically influence nanolayered thin films of barium fluoride, europium oxide, and aluminum oxide synthesized via pulsed laser deposition. Samples were synthesized with two different amounts of manganese, one with a 1:8 Mn to Eu ratio (0.5 nm MnO) and one with a 1:2 Mn to Eu ratio (2.0 nm MnO) based on projected deposited material thickness. The 1:8 Mn to Eu ratio sample showed no change in emission trends when compared to a sample singly doped with europium. The 1:2 Mn to Eu ratio exhibited a new emission at 448 nm that was not found in the other samples. The altered emission resulted in a blue-shift in the chromic coordinates (x= 0.23, y=0.26), which could be advantageous for applications with UV-pumped blue-light LEDs. The emission intensity of both samples was steady when exposed to a UV excitation laser.

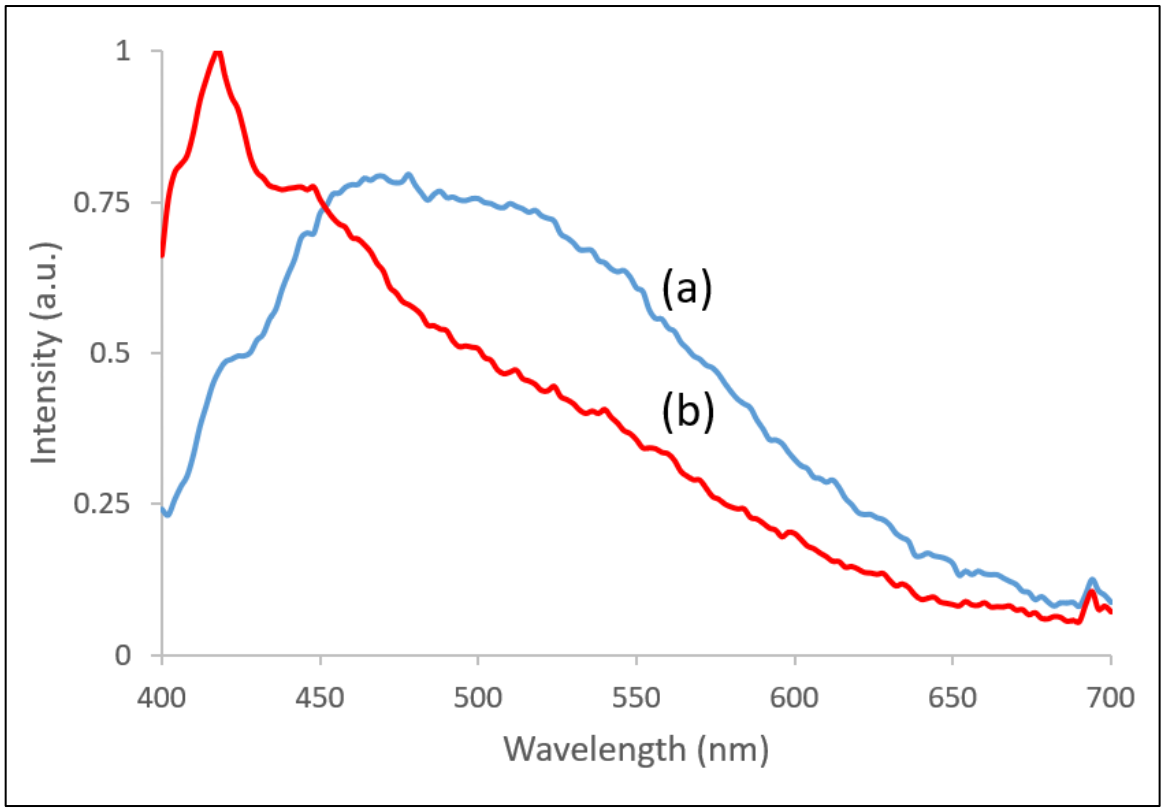

Figure 33. Emission spectra of the 0.5 nm MnO sample after a 1-hour heat treatment at 300 °C in (a) a nitrogen atmosphere and (b) as-made. A 355 nm excitation source was used.

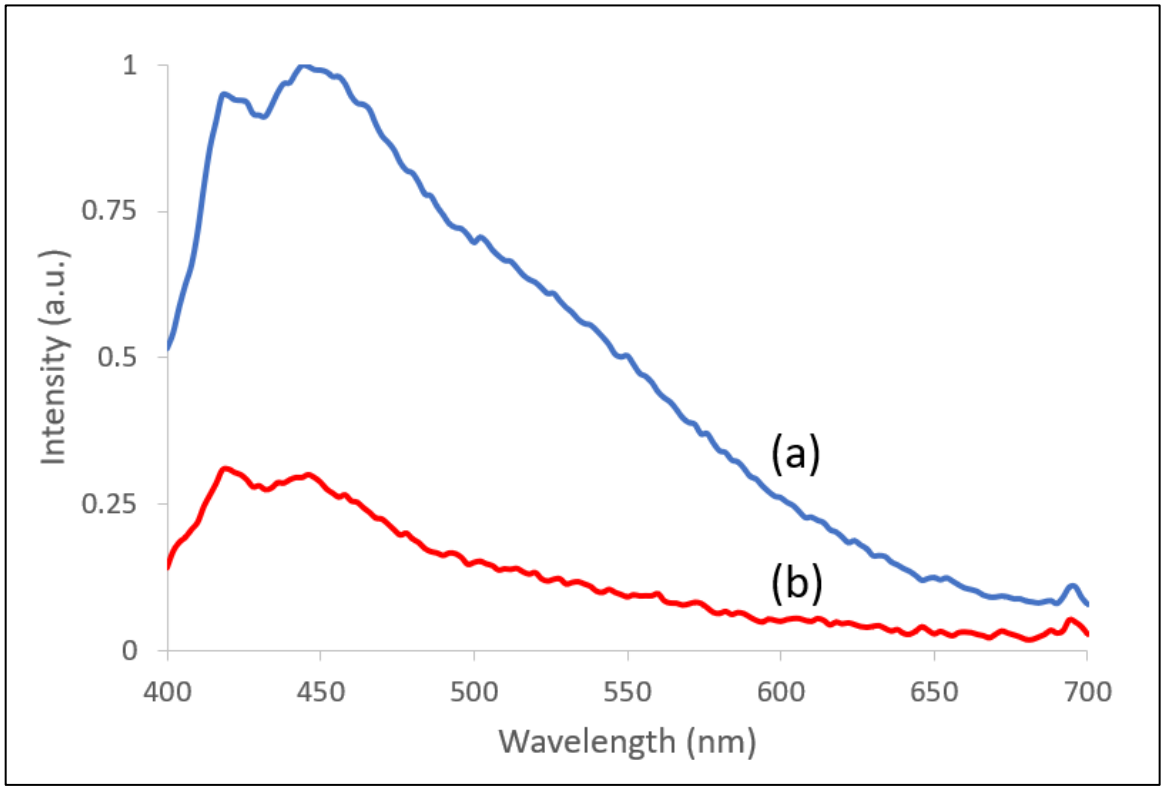

Figure 34. Emission spectra of the 2 nm MnO sample after a 1-hour heat treatment at 300 °C in (a) a nitrogen atmosphere and (b) as-made. A 355 nm excitation source was used.

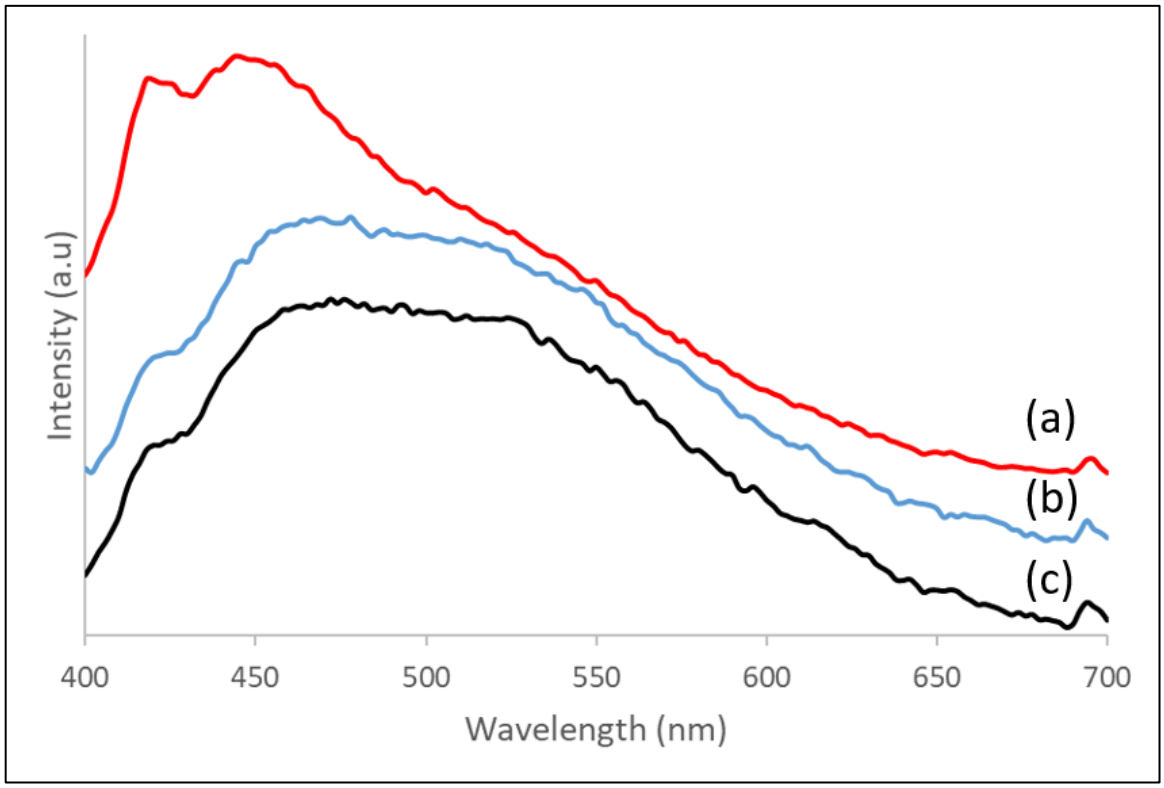

Figure 35. Emission spectra of (a) 2 nm MnO sample, (b) 0.5 nm MnO sample, and (c) sample without Mn. All samples were heat treated for 1-hour at 300 °C in a nitrogen atmosphere. A 355 nm excitation source was used.

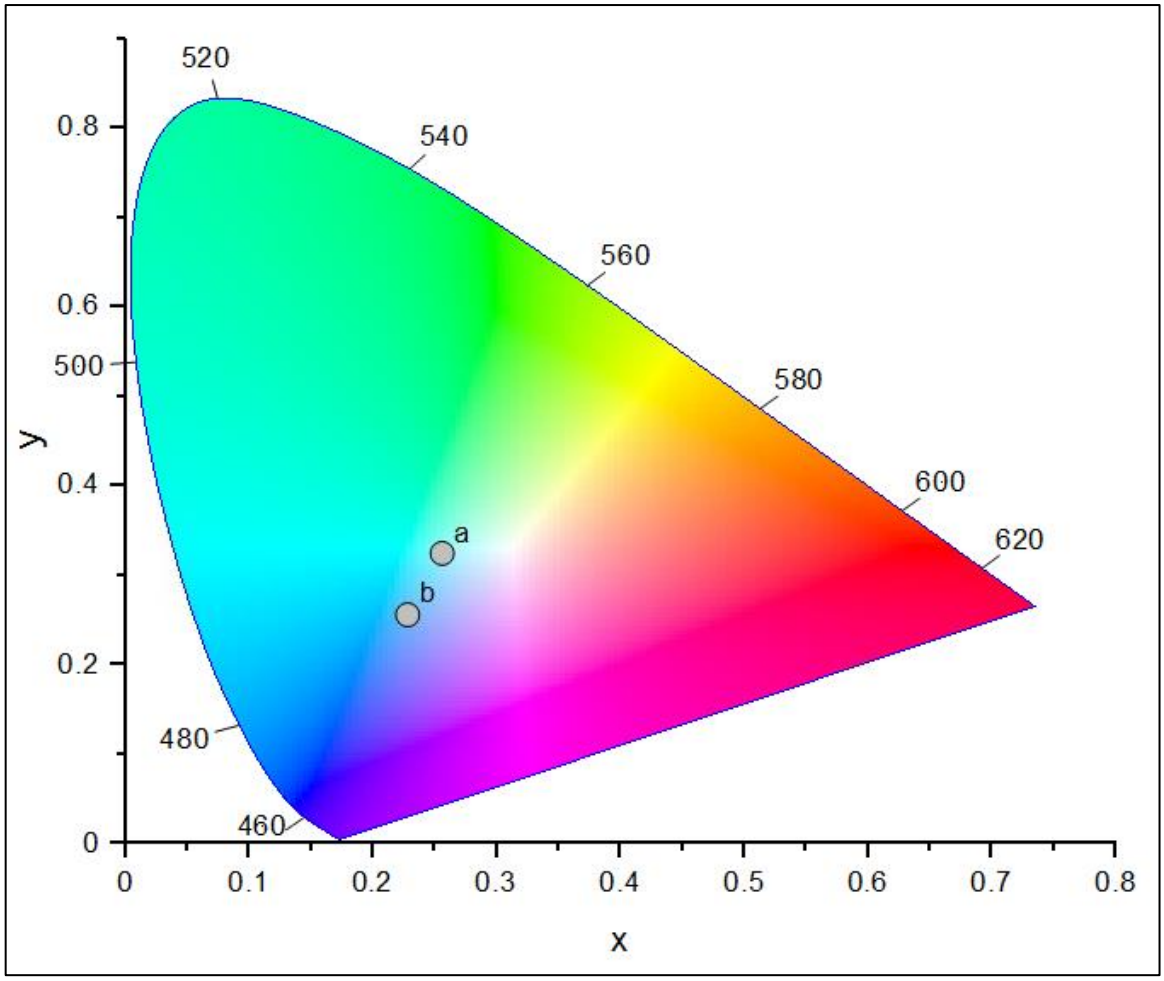

Figure 36. Color points in the CIE 1931 chromaticity diagram of the (a) 0.5 nm MnO sample and the (b) 2 nm MnO sample after a 1-hour heat treatment at 300 °C in a nitrogen atmosphere.

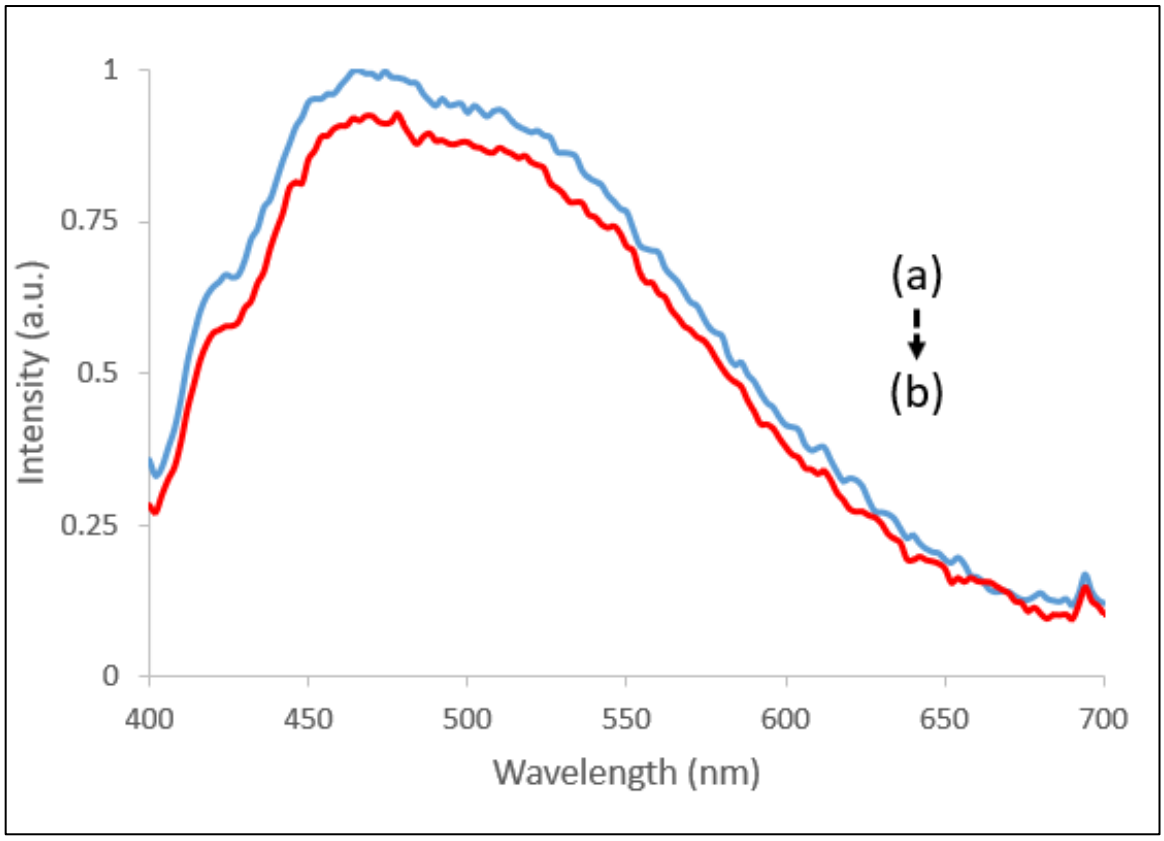

Figure 37. Emission spectra of the 0.5 nm MnO sample from a 355 nm excitation source after a 1-hour post-synthesis heat treatment in a nitrogen atmosphere. The spectra were contained from consecutive measurements of the same sample location. Spectrum (a) is the first measurement and (b) is the second measurement.

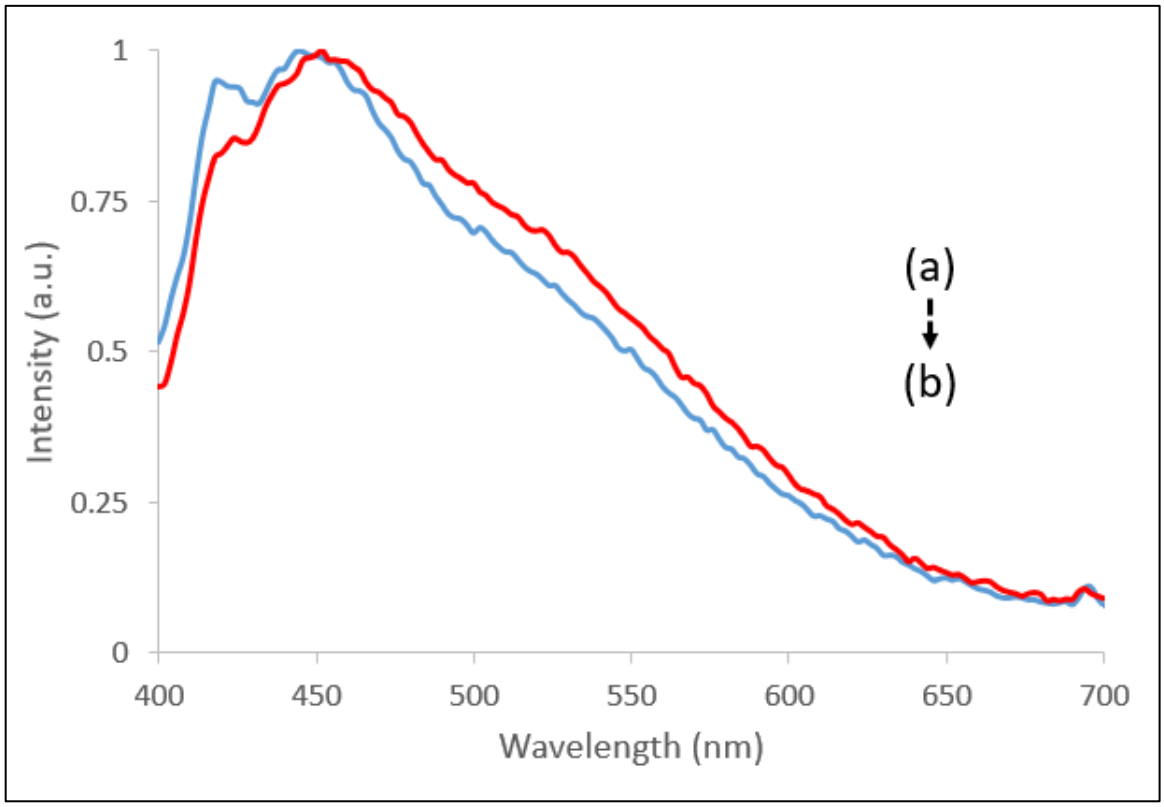

Figure 38. Emission spectra of the 0.5 nm MnO sample from a 355 nm excitation source after a 1-hour post-synthesis heat treatment in a nitrogen atmosphere. The spectra were contained from consecutive measurements of the same sample location. Spectrum (a) is the first measurement and (b) is the second measurement.

CONCLUSION

Optically active films were successfully synthesized via pulsed laser deposition and evaluated for applications in computed radiography or light-emitting diodes. The films were comprised of a halide crystal, a europium dopant, and an amorphous matrix material. The structural and optical characteristics of these films were dependent on target materials, pulsed laser deposition parameters, and post synthesis thermal treatments. The optical performance of the films for biomedical applications was determined.

The incorporation of $BaCl_2:Eu^{2+}$ crystallites into an amorphous matrix was confirmed in approximately 13 μm films via x-ray diffraction. The films' storage phosphor capability was determined with the analysis of photostimulated luminescence. The investigation of two different amorphous matrices (Si and SiO_2) revealed that both materials make a suitable host for the crystallites. A radiograph was developed using computed radiography and an experimental film that demonstrated a spatial resolution of 10 lp/mm, which is commercially considered to be high-resolution. The conversion efficiency of a commercial BFB storage phosphor plate was superior to that of the experimental storage phosphor films demonstrating a lack of practicality in medical imaging. However, for applications such as nondestructive testing, in which dose is not critical, the CE would be of lesser concern. This synthesis technique has the ability to be applied to the creation of scintillating glass-ceramic substrates that can be used in indirect flat panel detectors. A prototype has been made, but additional material investigation must be conducted to improve scintillating efficiency.

The nanolayered configuration of BaF_2/ Eu_2O_3/ Al_2O_3 films was shown to influence their optical properties due to the europium dopant being in different coordinate environments. Three layered configurations were synthesized and optically characterized following different post-synthesis heat treatment procedures. Cross-section TEM showed that layers of each material were deposited as continuous, uniform layers. Films subject to ambient atmosphere heat-treatments exhibited emission degradation when subject to an excitation

laser. However, it is found that with heat treatments in a nitrogen atmosphere, this degradation can be suppressed. All sample structures demonstrated the potential for applications in UV-pumped white light LEDs. Manganese was used to synthesize codoped samples, and a threshold for the amount of Mn necessary to optically influence the nanolayered films was determined.

Nanoscale control of synthesizing optically active thin films was demonstrated using pulsed laser deposition. The effects of differing nanostructures on optical properties that were determined can led to improvements in biomedical applications such as medical imaging and photobiomodulation.

REFERENCES

1. Ritenour, E.R., *Physics overview of screen-film radiography.* Radiographics, 1996. **16**(4): p. 903-16.

2. Bansal, G.J., *Digital radiography. A comparison with modern conventional imaging.* Postgraduate medical journal, 2006. **82**(969): p. 425-428.

3. Korner, M., et al., *Advances in digital radiography: Physical principles and system overview.* Radiographics, 2007. **27**(3): p. 675-686.

4. Chotas, H.G., J.T. Dobbins, and C.E. Ravin, *Principles of digital radiography with large-area, electronically readable detectors: A review of the basics.* Radiology, 1999. **210**(3): p. 595-599.

5. Fujita, H., et al., *Basic imaging properties of a computed radiographic system with photostimulable phosphors.* Med Phys, 1989. **16**(1): p. 52-9.

6. H, K. *Photostimulable phosphor radiography design considerations*. in *Specification, Acceptance Testing, and Quality Control of Diagnostic X-Ray Imaging Equipment*. 1994.

7. Rowlands, J.A., *The physics of computed radiography.* Physics in Medicine and Biology, 2002. **47**(23): p. R123-R166.

8. Blasse, G. and B.C. Grabmaier, *Luminescent materials*. 1994, Berlin; New York: Springer-Verlag.

9. Thoms, M., H. Vonseggern, and A. Winnacker, *Spatial Correlation and Photostimulability of Defect Centers in the X-ray-storage Phosphor BaFBr-Eu^{2+}*. Physical Review B, 1991. **44**(17): p. 9240-9247.

10. Fouassier, C., *Luminescent materials.* Current Opinion in Solid State and Materials Science, 1997. **2**(2): p. 231-235.

11. Leonard, R.L., A.R. Lubinsky, and J.A. Johnson, *The effects of sodium fluoride content on the properties of fluorochlorozirconate glass-ceramic storage phosphors.* Journal of the American Ceramic Society, 2017. **100**(4): p. 1551-1560.

12. Wierer, J.J., et al., *High-power AlGaInN flip-chip light-emitting diodes.* Applied Physics Letters, 2001. **78**(22): p. 3379-3381.

13. Cho, J., et al., *White light-emitting diodes: History, progress, and future.* Laser & Photonics Reviews, 2017. **11**(2).

14. Haitz, R.K., Fred; Tsao, Jeff; Nelson, Jeff *The Case for a National Research Program on Semiconductor Lighting*, in *Sandia Report*. 2000, Sandia National Laboratories.

15. Schubert, E.F. and J.K. Kim, *Solid-state light sources getting smart.* Science, 2005. **308**(5726): p. 1274-1278.

16. Bergh, A., et al., *The promise and challenge of solid-state lighting.* Physics Today, 2001. **54**(12): p. 42-47.

17. Dong, J.F. and D.X. Xiong, *Applications of Light Emitting Diodes in Health Care.* Annals of Biomedical Engineering, 2017. **45**(11): p. 2509-2523.

18. van Bommel, W.J.M., *Non-visual biological effect of lighting and the practical meaning for lighting for work.* Applied Ergonomics, 2006. **37**(4): p. 461-466.

19. Orsinger, G.V., et al., *Simultaneous multiplane imaging of human ovarian cancer by volume holographic imaging.* Journal of Biomedical Optics, 2014. **19**(3).

20. Pigula, A., et al., *Video-rate dual polarization multispectral endoscopic imaging*. SPIE BiOS. Vol. 9333. 2015: SPIE.

21. Barolet, D., *Light-Emitting Diodes (LEDs) in Dermatology.* Seminars in Cutaneous Medicine and Surgery, 2008. **27**(4): p. 227-238.

22. Ohring, M., *Chapter 3 - Thin-Film Evaporation Processes*, in *Materials Science of Thin Films (Second Edition)*. 2002, Academic Press: San Diego. p. 95-144.

23. Lowndes, D.H., et al., *Synthesis of novel thin-film materials by pulsed laser deposition.* Science, 1996. **273**(5277): p. 898-903.

24. Rao, M.C. *Pulsed Laser Deposition — Ablation Mechanism and Applications*. 2013.

25. Schweizer, S., A.R. Lubinsky, and J.A. Johnson, *Fluorozirconate-based glass-ceramic storage phosphors for digital mammography*, in *Medical Imaging 2007: Physics of Medical Imaging, Pts 1-3*, J. Hsieh and M.J. Flynn, Editors. 2007.

26. Wang, B., et al., *Photostimulated near-infrared persistent luminescence Cr^{3+}-doped Zn-Ga-Ge-O phosphor with high QE for optical information storage.* Journal of Alloys and Compounds, 2020. **812**.

27. Gu, M., X. Li, and Y. Cao, *Optical storage arrays: a perspective for future big data storage.* Light: Science & Applications, 2014. **3**(5): p. e177-e177.

28. Schweizer, S., *Physics and current understanding of X-ray storage phosphors.* Physica Status Solidi A-Applications and Materials Science, 2001. **187**(2): p. 335-393.

29. Hu, T., et al., *Color-tunable persistent luminescence in oxyfluoride glass and glass ceramic containing Mn^{2+}:alpha-Zn_2SiO_4 nanocrystals.* Journal of Materials Chemistry C, 2017. **5**(6): p. 1479-1487.

30. Zhuang, Y.X., et al., *Optical Data Storage and Multicolor Emission Readout on Flexible Films Using Deep-Trap Persistent Luminescence Materials.* Advanced Functional Materials, 2018. **28**(8).

31. Johnson, J.A., S. Schweizer, and A.R. Lubinsky, *A glass-ceramic plate for mammography.* Journal of the American Ceramic Society, 2007. **90**(3): p. 693-698.

32. Leonard, R.L., et al., *Evaluation of a Fluorochlorozirconate Glass-Ceramic Storage Phosphor Plate for Gamma-Ray Computed Radiography.* Journal of the American Ceramic Society, 2015. **98**(8): p. 2541-2547.

33. Huda, W., L.N. Rill, and A.P. Bruner, *Relative speeds of Kodak computed radiography phosphors and screen-film systems.* Medical Physics, 1997. **24**(10): p. 1621-1628.

34. Sonoda, M., et al., *Computed Radiography Utilizing Scanning Laser Stimulated Luminescence.* Radiology, 1983. **148**(3): p. 833-838.

35. Nanto, H., et al., *X-ray imaging plate using CsBr : Eu phosphors for computed radiography.* Nuclear Instruments & Methods in Physics Research Section a-Accelerators Spectrometers Detectors and Associated Equipment, 2007. **580**(1): p. 278-281.

36. Schweizer, S.R., U; Assmann, S; Spaeth, JM, *RbBr and CsBr doped with Eu^{2+} as new competitive X-ray storage phosphors.* Radiation Measurements, 2001. **33**(5): p. 483 - 486.

37. Leblans, P., D. Vandenbroucke, and P. Willems, *Storage Phosphors for Medical Imaging.* Materials (Basel, Switzerland), 2011. **4**(6): p. 1034-1086.

38. Vonseggern, H., *X-ray-imaging with Photostimulable Phosphors.* Nuclear Instruments & Methods in Physics Research Section a-Accelerators Spectrometers Detectors and Associated Equipment, 1992. **322**(3): p. 467-471.

39. Alvarez, C.J., et al., *Structural and Kinetic Analysis of $BaCl_2$ Nanocrystals in Fluorochlorozirconate Glass-Ceramics.* Journal of the American Ceramic Society, 2015. **98**(4): p. 1099-1104.

40. Evans, A.W., et al., *The effect of trivalent iron on the properties of fluorochlorozirconate glass ceramics.* Journal of Non-Crystalline Solids, 2018. **484**: p. 8-13.

41. Selling, J., et al., *Comparison of the luminescence properties of the x-ray storage phosphors $BaCl_2 : Ce^{3+}$ and $BaBr_2 : Ce$.* Journal of Physics-Condensed Matter, 2005. **17**(50): p. 8069-8078.

42. Appleby, G.A., et al., *Photostimulated luminescence from $BaCl_2 : Eu^{2+}$ nanocrystals in lithium borate glasses following neutron irradiation.* Applied Physics Letters, 2006. **89**(10).

43. Appleby, G.A. and P. Vontobel, *Optimisation of lithium borate-barium chloride glass-ceramic thermal neutron imaging plates.* Nuclear Instruments & Methods in Physics Research Section a-Accelerators Spectrometers Detectors and Associated Equipment, 2008. **594**(2): p. 253-256.

44. Schweizer, S., et al., *Photostimulated luminescence in Eu-doped fluorochlorozirconate glass ceramics.* Applied Physics Letters, 2003. **83**(3): p. 449-451.

45. Chen, G., et al., *Fluorozirconate-based nanophase glass ceramics for high-resolution medical X-ray imaging.* Journal of Non-Crystalline Solids, 2006. **352**(6-7): p. 610-614.

46. Bond, C.W., et al., *Pulsed laser deposition of transparent fluoride glass.* Journal of Non-Crystalline Solids, 2018. **488**: p. 19-23.

47. Alvarez, C.J., et al., *Nanocrystallization in Fluorochlorozirconate Glass-Ceramics.* Journal of the American Ceramic Society, 2013. **96**(11): p. 3617-3621.

48. Cadieu, F.J., et al., *Inplane Magnetized Yig Substrates Self-biased By SmCo Based Sputtered Film Coatings.* Journal of Applied Physics, 1994. **76**(10): p. 6059-6061.

49. Cadieu, F.J., et al., *High coercivity SmCo based films made by pulsed laser deposition.* Journal of Applied Physics, 1998. **83**(11): p. 6247-6249.

50. Beutel, J., et al., *Handbook of medical imaging. Volume 1, Volume 1*. 2000.

51. Lubinsky, A.R., et al., *Scanning translucent glass-ceramic x-ray storage phosphors*, in *Medical Imaging 2010: Physics of Medical Imaging*, E. Samei and N.J. Pelc, Editors. 2010.

52. Koughia, C., et al., *Samarium-Doped Fluorochlorozirconate Glass-Ceramics as Red-Emitting X-Ray Phosphors.* Journal of the American Ceramic Society, 2011. **94**(2): p. 543-550.

53. Pei, Z.L., et al., *Luminescence property of Eu-doped fluorochlorozirconate glass-ceramics.* Journal of Rare Earths, 2009. **27**(2): p. 338-340.

54. Selling, J., et al., *Europium-doped barium halide X-ray scintillators.* physica status solidi c, 2007. **4**(3): p. 976-979.

55. Ziyuan, W., et al., *Blue-shift of Eu^{2+} emission in $(Ba,Sr)_3Lu(PO_4)_3:Eu^{2+}$ eulytite solid-solution phosphors resulting from release of neighbouring-cation-induced stress.* Dalton transactions (Cambridge, England : 2003), 2014. **43**.

56. Shang, M.M., C.X. Li, and J. Lin, *How to produce white light in a single-phase host?* Chemical Society Reviews, 2014. **43**(5): p. 1372-1386.

57. Bendersky, L.A., et al., *Structural Studies of Pulsed-laser-deposited $Ba_4Fe_4Ti_3O_{16}$ Oxide Films.* Journal of Materials Research, 2000. **15**(6): p. 1389-1396.

58. Buchanan, A., et al., *Perception versus reality-findings from a phosphor plate quality assurance study.* Oral Surgery Oral Medicine Oral Pathology Oral Radiology, 2017. **123**(4): p. 496-501.

59. Leonard, R.L., et al., *Scintillating glass-ceramic substrates for indirect flat panel detectors in digital radiography.* Journal of the American Ceramic Society, 2020. **103**(12): p. 6893-6900.

60. Guo, H., et al., *Preparation, structural and luminescent properties of $Ba_2Gd_2Si_4O_{13}:Eu^{3+}$ for white LEDs.* Optics Express, 2011. **19**(6): p. A201-A206.

61. He, S.G., et al., *A Mn^{4+}-doped oxyfluoride phosphor with remarkable negative thermal quenching and high color stability for warm WLEDs.* Chemical Engineering Journal, 2020. **392**.

62. Lin, C.C. and R.S. Liu, *Advances in Phosphors for Light-emitting Diodes.* Journal of Physical Chemistry Letters, 2011. **2**(11): p. 1268-1277.

63. Guo, H., et al., *Ultraviolet light induced white light emission in Ag and Eu^{3+} co-doped oxyfluoride glasses.* Optics Express, 2010. **18**(18): p. 18900-18905.

64. Kim, J.S., et al., *White-light generation through ultraviolet-emitting diode and white-emitting phosphor.* Applied Physics Letters, 2004. **85**(17): p. 3696-3698.

65. Gong, Y., et al., *Ce^{3+},Dy^{3+} Co-Doped White-Light Long-Lasting Phosphor: $Sr_2Al_2SiO_7$ Through Energy Transfer.* Journal of the Electrochemical Society, 2010. **157**(6): p. J208-J211.

66. Sheu, J.K., et al., *Warm-white light-emitting diode with high color rendering index fabricated by combining trichromatic InGaN emitter with single red phosphor.* Optics Express, 2015. **23**(7): p. A232-A239.

67. Bouchard, M.B., et al., *Ultra-fast multispectral optical imaging of cortical oxygenation, blood flow, and intracellular calcium dynamics.* Optics Express, 2009. **17**(18): p. 15670-15678.

68. Clancy, N.T., et al., *Development and evaluation of a light emitting diode endoscopic light source*, in *Advanced Biomedical and Clinical Diagnostic Systems X*, T. VoDinh, A. MahadevanJansen, and W.S. Grundfest, Editors. 2012.

69. Hennessy, M. and M.R. Hamblin, *Photobiomodulation and the brain: a new paradigm.* Journal of Optics, 2017. **19**(1).

70. Sohn, H., et al., *Effects of Light-Emitting Diode Irradiation on RANKL-Induced Osteoclastogenesis.* Lasers in Surgery and Medicine, 2015. **47**(9): p. 745-755.

71. Mao, Z.Y., et al., *Tunable single-doped single-host full-color-emitting $LaAlO_3$: Eu phosphor via valence state-controlled means.* Chemical Communications, 2009(3): p. 346-348.

72. Wu, Z.C., et al., *A new single-host white-light-emitting $BaSrMg(PO_4)_2$: Eu^{2+} phosphor for white-light-emitting diodes.* Journal of Alloys and Compounds, 2010. **498**(2): p. 139-142.

73. Aull, B.F. and H.P. Jenssen, *Impact of Ion-Host Interactions on the 5d-to-4f Spectra of Lanthanide Rare-Earth-Metal Ions .1. A Phenomenological Crystal-Field Model.* Physical Review B, 1986. **34**(10): p. 6640-6646.

74. Leonard, R.L., et al., *Rare earth doped downshifting glass ceramics for photovoltaic applications.* Journal of Non-Crystalline Solids, 2013. **366**: p. 1-5.

75. Zhao, J.J., et al., *Structural Origins of $BaF_2/Ba_{1-x}R_xF_{2+x}/RF_3$ Nanocrystals Formation from Phase Separated Fluoroaluminosilicate Glass: A Molecular Dynamic Simulation Study.* Advanced Theory and Simulations, 2019. **2**(10).

76. Dejneka, M., *The luminescence and structure of novel transparent oxyfluoride glass-ceramics.* Journal of Non-Crystalline Solids, 1998. **239**(1-3): p. 149-155.

77. Fang, Z.J., et al., *Phase-Separation Engineering of Glass for Drastic Enhancement of Upconversion Luminescence.* Advanced Optical Materials, 2019. **7**(8).

78. Camps, I., A. Mariscal, and R. Serna, *Preparation and broadband white emission of Eu-doped thin films based on SiAlON.* Journal of Luminescence, 2017. **191**: p. 97-101.

79. Zhang, Q., et al., *Reduction of Eu^{3+} to Eu^{2+} in Eu-doped high silica glass prepared in air atmosphere.* Optical Materials, 2010. **32**(3): p. 427-431.

80. Hu, G.X., et al., *Regulation of luminescence properties of SBGNA:Eu^{3+} glass by the content of B_2O_3 and Al_2O_3.* Optical Materials, 2020. **106**.

81. Howe, B. and A.L. Diaz, *Characterization of host-lattice emission and energy transfer in $BaMgAl_{10}O_{17} : Eu^{2+}$*. Journal of Luminescence, 2004. **109**(1): p. 51-59.

82. Dawson, B., et al., *Mechanisms of VUV damage in $BaMgAl_{10}O_{17} : Eu^{2+}$*. Chemistry of Materials, 2004. **16**(25): p. 5311-5317.

83. Amidani, L., et al., *Oxidation and Luminescence Quenching of Europium in $BaMgAI_{10}O_{17}$ Blue Phosphors.* Chemistry of Materials, 2017. **29**(23): p. 10122-10129.

84. Choi, W.S., et al., *Wide bandgap tunability in complex transition metal oxides by site-specific substitution.* Nature Communications, 2012. **3**.

85. Capasso, F., *Band-Gap Engineering - From Physics and Materials to New Semiconductor-Devices.* Science, 1987. **235**(4785): p. 172-176.

86. Zhang, X.G., et al., *Dopant preferential site occupation and high efficiency white emission in $K_2BaCa(PO_4)_2:Eu^{2+},Mn^{2+}$ phosphors for high quality white LED applications.* Inorganic Chemistry Frontiers, 2019. **6**(5): p. 1289-1298.

87. Wu, L.W., et al., *Analysis of the structure and abnormal photoluminescence of a red-emitting $LiMgBO_3:Mn^{2+}$ phosphor.* Dalton Transactions, 2018. **47**(37): p. 13094-13105.

88. Cotton, F.A., *Chemical applications of group theory*. 1990, New York: Wiley.

89. Yang, W.J., et al., *Luminescence and energy transfer of Eu- and Mn-coactivated $CaAl_2Si_2O_8$ as a potential phosphor for white-light UVLED.* Chemistry of Materials, 2005. **17**(15): p. 3883-3888.

90. Caldino, U., A. Munoz, and J. Rubio, *Luminescence and Energy-Transfer in CaF_2 Slightly Doped with Europium and Manganese.* Journal of Physics-Condensed Matter, 1990. **2**(27): p. 6071-6078.

91. Caldino, U.G., A.F. Munoz, and J.O. Rubio, *Energy-transfer in $CaCl_2$-Eu-Mn Crystals.* Journal of Physics-Condensed Matter, 1993. **5**(14): p. 2195-2202.

92. Mendez, A., et al., *Energy transfer mechanisms in the KBr : Eu^{2+}: Mn^{2+} phosphor*. Journal of Materials Science Letters, 1999. **18**(5): p. 399-402.

93. Rubio, J., A. Munoz, and J. Garcia, *Energy-transfer Between Europium and Manganese Close Pairs in Monocrystalline Sodium-Bromide.* Physical Review B, 1987. **36**(15): p. 8115-8121.

94. Rubio, J., et al., *Eu^{2+}- Mn^{2+} Energy-Transfer in NaCl.* Physical Review B, 1985. **31**(1): p. 59-67.

95. Camarillo, E. and J. Rubio, *A Spectroscopic Study of NaI Containing Europium and Manganese.* Journal of Physics-Condensed Matter, 1989. **1**(30): p. 4873-4883.

96. Chen, J., et al., *Emission red shift and energy transfer behavior of color-tunable $KMg_4(PO_4)_3$:Eu^{2+},Mn^{2+} phosphors.* Journal of Materials Chemistry C, 2015. **3**(21): p. 5516-5523.

97. Yu, J.Y., et al., *A new emission band of Eu^{2+} and its efficient energy transfer to Mn^{2+} in $Sr_2Mg_3P_4O_{15}$:Mn^{2+}, Eu^{2+}*. Chemical Communications, 2011. **47**(45): p. 12376-12378.

98. Karuppaiah, M., et al., *Rapid microwave assisted synthesis of Mn_2O_3 and Co_3O_4 nanoparticles and their structural, optical and magnetic properties*. 2018.

99. Kashir, A., et al., *Pulsed Laser Deposition of Rocksalt Magnetic Binary Oxides.* Thin Solid Films, 2019. **692**.

100. Fritsch, S. and A. Navrotsky, *Thermodynamic properties of manganese oxides.* Journal of the American Ceramic Society, 1996. **79**(7): p. 1761-1768.

101. Du, J.R., et al., *$LaAlO_3$:Mn^{4+} as Near-Infrared Emitting Persistent Luminescence Phosphor for Medical Imaging: A Charge Compensation Study.* Materials, 2017. **10**(12).

102. Jansen, T., F. Baur, and T. Jüstel, *Red emitting $K_2NbF_7:Mn^{4+}$ and $K_2TaF_7:Mn^{4+}$ for warm-white LED applications.* Journal of Luminescence, 2017. **192**.

103. Teixeira, V.C., P.J.R. Montes, and M.E.G. Valerio, *Structural and optical characterizations of $Ca_2Al_2SiO_7:Ce^{3+}$, Mn^{2+} nanoparticles produced via a hybrid route.* Optical Materials, 2014. **36**(9): p. 1580-1590.

104. Chellappa, S.L., et al., *Non-Visual Effects of Light on Melatonin, Alertness and Cognitive Performance: Can Blue-Enriched Light Keep Us Alert?* Plos One, 2011. **6**(1).

VITA

Charles William Bond was born in Tullahoma, Tennessee to David and Tina Bond. He has a younger sister, Paige, and an older brother, Chris. He obtained his Bachelor of Science Degree in Chemistry at University of the Cumberlands and his Master of Science Degree from The University of Tennessee in Biomedical Engineering in 2018. Charles obtained his Doctor of Philosophy Degree from The University of Tennessee in Biomedical Engineering in 2021.